ERDC/GSL TR-12-30

Geotechnical and Structures Laboratory

US Army Corps
of Engineers®
Engineer Research and
Development Center

Multiscale Modeling of the Structure of Material

Modeling Nanomechanical Behavior of Calcium-Silicate-Hydrate

Mei Qiang Chandler, John F. Peters, and Daniele Pelessone

August 2012

ERDC/GSL TR-12-30
August 2012

Modeling Nanomechanical Behavior of Calcium-Silicate-Hydrate

Mei Qiang Chandler and John F. Peters

Geotechnical and Structures Laboratory
U.S. Army Engineer Research and Development Center
3909 Halls Ferry Road
Vicksburg, MS 39180

Daniele Pelessone

Engineering and Software System Solutions, Inc
550 West "C" Street, Suite 1630
San Diego, CA, 92101, USA

Final report

Prepared for U.S. Army Corps of Engineers
441 G Street NW
Washington, DC 20314-1000

Under Work Unit 149289

Abstract

The Discrete Element Method (DEM) was used to model the nanomechanical behavior of Calcium-Silicate-Hydrate (C-S-H). The inter-particle forces consist of the traditional friction and contact forces that operate in granular materials, with the addition of nanometer-scale forces between gels, including van der Waals and ionic correlation forces. The contact normal forces were based on the Hertz contact law. The van der Waals attractive forces were calculated based on Hamaker's equation. The ionic correlation forces, generated from the negative charges on the C-S-H gel surface and the ion species in the pore solution, were calculated using Monte Carlo (MC) simulations. The particles are spherical with diameters of approximately five nano-meters. Virtual nanoindentation was performed to evaluate the elastic modulus and hardness of C-S-H nanoparticle assemblies. Both elastic modulus and hardness, calculated from DEM, were much smaller than the results from nanoindentation experiments for corresponding C-S-H nanoparticle packing densities. By using a higher rotational stiffness, both bulk modulus and hardness increase and they match well with the experimental data, pointing to the possibility that the morphology of C-S-H is far from a perfect sphere and interlocking between particles provides significant strength to C-S-H. These studies show that the elastic modulus of a C-S-H matrix increases with increased packing ratio and rotational resistance, and its hardness increases with increased packing ratio, cohesion, rotational resistance and shear friction coefficient. The studies also show that the elastic properties of an individual C-S-H nanoparticle have little effect on the elastic modulus and hardness of the C-S-H matrix. The studies suggest that increasing packing density of the C-S-H nanostructure is a favorable way of making the C-S-H matrix stiffer. Increasing packing density, the cohesion and shear friction coefficient is effective in making the C-S-H matrix stronger. However, increasing packing density also makes the material response more brittle.

Contents

Abstract ii

List of Figures and Tables iv

Preface vi

1 Introduction 1

1.1 Background 1
1.2 Research objectives 2

2 Discrete Element Modeling of C-S-H 4

2.1 Introduction 4
2.2 An overview of nanoindentation tests 5
2.3 Nanoindentation tests of C-S-H 8
2.4 Discrete Element Method (DEM) 9
2.5 Interparticle forces 10
2.5.1 C-S-H bonding force 10
2.5.2 Normal contact force 15
2.5.3 Net normal force 16
2.5.4 Tangential contact force 17
2.5.5 Rolling contact resistance 18
2.6 Particle generation 19
2.7 DEM model set up and parameters 20
2.8 Results and discussion 21

3 Parametric Studies 24

3.1 Introduction 24
3.2 Effects of rotational stiffness 24
3.3 Effects of normal cohesive force 28
3.4 Effects of sliding friction coefficient 31
3.5 Effects of elastic properties of C-S-H nanoparticles 34
3.6 A summary of the effects of different parameters on C-S-H matrix properties 37
3.7 Conclusion 39

4 Summary 40

References 41

Report Documentation Page

Figures and Tables

Figures

Figure1. A schematic of the research framework. 3

Figure 2. A schematic representation of the cross section of the indenter where "*a*" represents the indenter, "*b*" represents the surface of residual plastic indentation depth in the test specimen, and "*c*" represents the surface of the specimen at maximum depth 6

Figure 3. A typical force versus depth indentation curve where "a_c" is the loading curve, "b_c" is the unloading curve, and "c_c" is tangent to curve "b_c" at maximum load 7

Figure 4. A step, called pop-in, in the force-displacement curve from a nanoindentation test that corresponds to a crack formation in the indented material. 7

Figure 5. Load displacement curves from nanoindentation tests on C-S-H phases and quartz in hardened cement paste samples. 8

Figure 6. MC simulation result showing that the calcium ions accumulate between negatively-charged C-S-H nanoparticles. The large blue particles represent the C-S-H nanoparticle, small red particles represent the calcium ions, and small green particles represent hydroxyl ions. 12

Figure 7. Monte Carlo simulation results showing the average ionic correlation force between two nanoparticles in pore solutions versus the gap between two nanoparticles at different surface charging density. 13

Figure 8. Van der Waals force versus gap between a pair of C-S-H nanoparticles. 15

Figure 9. A schematic of two spheres in contact. 15

Figure 10. The normal interparticle forces versus gap between two nanoparticles. 17

Figure 11. The particle arrangements for three packing ratios i.e., (a) random packing (packing ratio $\approx$ 0.56), (b) random packing (packing ratio $\approx$ 0.64), and (c) close dense packing (packing ratio=0.74). 19

Figure12. The C-S-H nanoparticle assembly and the Berkovich indenter in DEM simulations. 20

Figure 13. The indentation force versus indentation depth for specimens with packing ratios of 0.56, 0.64 and 0.74. The snap shots show the progression of indented particle assembly. The color shows the stresses in the vertical direction of the specimen. 22

Figure 14. Indentation force versus indentation depth for different rotational stiffness while other parameters stay constant for (a) Packing ratio of 0.56, (b) Packing ratio of 0.64, and (c) packing ratio=0.74. 26

Figure 15. Elastic modulus of C-S-H matrix from simulations increases drastically when the rotational stiffness is increased from 1e-4 to 1 nN.nm/rad for packing densities of 0.56 and 0.64. However, little increase occurs when the rotational stiffness is increased further. 27

Figure16. The hardness of C-S-H matrix from simulations increases drastically when the rotational stiffness increases from 1e-4 to 1 nN.nm/rad for packing densities of 0.56 and 065 while little increase in hardness is seen when the rotational stiffness is increased further. 27

Figure 17. Indentation force versus indentation depth for various normal cohesive forces, keeping other parameters as they are listed in Table 1 for (a) Packing ratio=0.56, (b) Packing ratio=0.64, and (c) packing ratio=0.74. 30

Figure 18. Elastic modulus of C-S-H matrix estimated from the data in Figure 17. 31

Figure 19. Hardness of C-S-H matrix estimated from the data in Figure 17. 31

Figure 20. Indentation force versus indentation depth for different values of sliding friction coefficient, while other parameters stay the same as that listed in Table 1, for (a) Packing ratio=0.56, (b) Packing ratio=0.64, and (c) packing ratio=0.74. 33

Figure 21. Elastic modulus of C-S-H matrix estimated from the data in Figure 20. 34

Figure 22. Hardness of C-S-H matrix estimated from the data in Figure 20. 34

Figure 23. Indentation force versus indentation depth for different particle elastic moduli, while other parameters stay the same as that listed in Table 1, for (a) Packing ratio=0.56 (b) Packing ratio=0.64, and (c) packing ratio=0.74. 36

Figure 24. Elastic modulus of C-S-H matrix estimated from the data in Figure 23. 37

Figure 25. Hardness of C-S-H matrix is estimated from the data in Figure 23. 37

Figure 26. The normalized increase in elastic modulus and hardness versus the normalized increase in packing density, cohesive force, sliding friction coefficient, rotational stiffness and particle elastic modulus. 39

Tables

Table 1. Parameters used in the initial DEM simulations. 21

Table 2. The indentation modulus and indentation hardness calculated from DEM results in Figure 14 and experimental results from Constantinides and Ulm, 2007, and Ulm et al. 2007). 23

Preface

This study was conducted under the Military Engineering Basic Research Program, Project Number, 149289, "Multiscale Modeling of Structure of Materials," sponsored by Headquarters, U.S. Army Corps of Engineers. The technical monitor was Dr. David A. Horner, Technical Director for Military Engineering, U.S. Army Engineer Research and Development Center (ERDC).

The research was performed by Dr. Mei Q. Chandler, ERDC Structural Mechanics Branch (SMB), Geosciences and Structures Division (GSD), Geotechnical and Structures Laboratory (GSL), Dr. John F. Peters, GSL, and Dr. Daniele Pelessone, Engineering and Software System Solutions, Inc.

At the time of the publication of this report, Dr. Gordon W. McMahon, was Chief, SMB; Bartley P. Durst, was Chief, GSD; Dr. William P. Grogan was Deputy Director, GSL; and Dr. David W. Pittman was Director, GSL.

COL Kevin J. Wilson was Commander and Executive Director of ERDC. Dr. Jeffery P. Holland was Director.

1 Introduction

1.1 Background

High Performance Concrete (HPC) material has high unconfined compressive strength ranging from 150 MPa to 400 MPa (30 ksi-60 ksi) and was experimentally demonstrated to be effective in thin-walled panels for force protection structural components (Cargile et al. 1993). To explore the potential of this material fully for use in warfighting efforts, it is important to develop effective and high-fidelity numerical simulation tools to model the material under extreme loads such as impact and penetration. HPC is a highly heterogeneous material. Its microstructure consists of hydrated cement paste, unhydrated cement particles, fine aggregates, steel or polymer fibers, and disconnected pores with sizes ranging from hundreds of nano-meters to a few nano-meters (Gatty et al. 2001). Calcium-Silicate-Hydrate (C-S-H) is the most important phase in the paste of HPC, accounts for up to 60 percent in volume in the hydrated cement paste, and is the glue that holds together all the components in the HPC (Dejong and Ulm 2007). Despite its dominate role in concrete, the material behavior and underlying failure mechanisms of C-S-H are poorly known. Therefore, studying the underlying failure mechanisms and material behavior of C-S-H is essential in modeling the HPC performances under impact and penetration loading conditions.

Based on experimental data from Atomic Force Microscope (AFM; Nonat 2004), small angle neutron scattering (SANS; Allen et al. 2007), Transmission Electron Microscope (TEM; Richardson 2004), and nanoindentation (Constantinides and Ulm 2007), the elementary building blocks of C-S-H are believed to be negatively-charged nanoparticles. Each C-S-H nanoparticle consists of C-S-H solid phase and chemically-bounded interlayer water (Allen et al. 2007). The C-S-H solid phase does not have a well-defined stoichiometry and may have tobermorite-like and jennite-like molecular structures (Nonat 2004). There is bulk water at the nanopores between nanoparticles and adsorbed water on the surface of C-S-H nanoparticles (Allen et al. 2007). The morphology of C-S-H nanoparticles is also ill defined. Gauffinet et al. (1998) suggested that C-S-H gels had lamellae-type morphologies with lamellae sizes of approximately 60 nm by 30 nm by 5 nm. Richardson (2004) and Jennings (2000, 2007) suggested that the morphology of C-S-H gels are globular with average diameters of

approximately 5 nm. The latest atomic simulations of the molecular structure of C-S-H (Pellenq et al. 2009) suggest that C-S-H molecular structures include silica monomer, silica chain chunks, and infinite silica chains, which perpetuate a C-S-H morphology and include possible long slender particles and globular-like particles.

Experiments (Constantinides and Ulm 2007) also suggest that C-S-H gels are packed into two different packing densities (low-density and high-density C-S-H) in the cement matrix. The nanoindentation experiments performed by Ulm et al. (2007) suggest that C-S-H behaves as a nano-granular medium, and both the elastic modulus and hardness of bulk C-S-H depends on the packing density of C-S-H gels. Jennings (2000) suggests that packing densities of low-density and high-density C-S-H are approximately 0.63 and 0.76, respectively. The statistic nanoindentation tests by Ulm et al. (2007) also show two distinctively different ranges of elastic modulus and hardness.

C-S-H nanostructure is characterized by a very high surface-area-to-volume ratio that promotes the interaction with water to provide cohesion for the C-S-H nanostructure (Pellenq et al. 2004, 2008). Gmire et al. (1998) further suggest that an ionic covalent bonding force exists between C-S-H solid layers. They also suggest that the interparticle forces between C-S-H nanoparticles might include mainly physical type bond forces (London vander Waals type) and less dominate chemical forces (ionic covalent type).

1.2 Research objectives

The Discrete Element Method (DEM; Cundall 1971) was used to investigate how well the structural characteristics and inter-particle forces proposed in the literature are consistent with physical properties measured in nanoindentation experiments. The structure of the C-S-H matrix is assumed to have a simple form with each C-S-H nanoparticle treated as a rigid particle that deforms at the contacts and interactions between nanoparticles driven by multiple interparticle forces. Monte Carlo (MC) simulations were performed to study the ionic correlation forces between ions in the nanopores and nanoparticle virtual nanoindentation simulations, and the results were compared to the experimental data (Constantinides and Ulm 2007) to correlate and validate the model. Failure mechanisms and constitutive relations of C-S-H at the submicron and micron scales were obtained by applying different loads to the discrete

element models of C-S-H nanoparticles. This information can then be incorporated into a finite element model as a matrix of cement paste at microscales. Those models can then be linked further to the mesoscale models. The ultimate goals are to understand how to improve the mechanical performance of the C-S-H material and provide a micromechanical interpretation to the constitutive laws that are used in blast and penetration simulations that include consideration of nanostructures, microstructures, and mesostructures of HPC. Figure 1 illustrates the research framework.

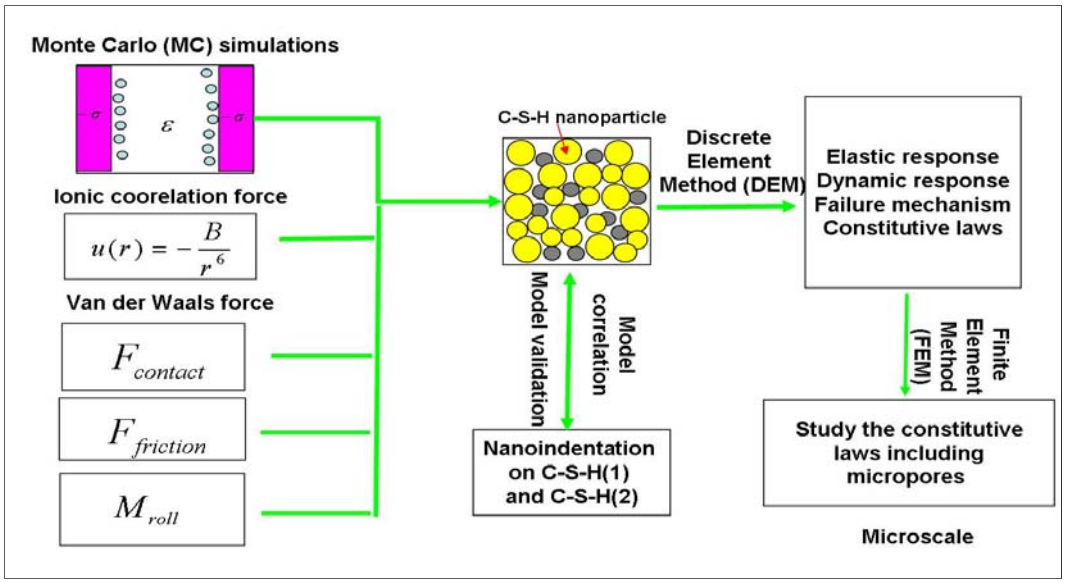

Figure1. A schematic of the research framework.

2 Discrete Element Modeling of C-S-H

2.1 Introduction

C-S-H nanoparticles are small-sized with the smallest dimension on the order of 5 nm (Jennings 2000 Richardson 2004), and are separated by water molecules in the C-S-H matrix. Material behavior is generally size-dependent (Horstemeyer et al. 2001). For example, research results (Shan et al. 2004) show that the plastic deformation mechanism of nanocrystalline nickel is mainly grain-boundary meditated, which includes grain-boundary sliding and grain rotation. Sen and Buehler (2009) also showed that few dislocation activities are present inside the nanocrystals under deformation because of geometric confinement imposed by the small size of the nanocrystals relative to the size of flaws. Similar examples come from studies of geologic materials (Anandarajah 1994). Research results from Yao and Anandarajah (2003) suggest that material behavior of clay depends on the arrangements and interactions between particles. The research on nanocrystalline materials points to a deformation mechanism similar to granular-type materials, in which deformation is controlled by the interaction between grains instead of deformation inside grains.

The Discrete Element Method (DEM) was used to model granular materials at the particle level as opposed to a continuum representation and was used successfully to study soils (Anandarajah 1994) and clays (Yao and Anandarajah 2003). In DEM models, the particles only deform, slide, and rotate at inter-particle contacts. The main parameters of DEM models are the shapes and sizes of the particles, the packing arrangement of particles, and interparticle forces between particles. In regular granular material models, interparticle forces usually include only contact forces. To model C-S-H nanostructure, nano-meter-scale forces, such as ionic forces and van der Waals forces, need to be included as well. The shape of C-S-H nanoparticles is still in debate. In the analyses reported here, spheres were used with nominal diameters of 5 nm to represent C-S-H nanoparticles for simplicity in corresponding to approximate globular morphology suggested by Jennings (2000 2007) and Richardson (2004). Rotational stiffness was applied in the model to account for resistance of rotations caused by the differences between perfect spheres and the actual globular shape. The packing arrangements of C-S-H nanoparticles depend

on particle sizes and shapes. In this work, the nanoparticles were arranged randomly with a packing ratio of approximately 0.64 to model a low-density C-S-H and with a packing ratio of 0.74 to model a high-density C-S-H. This facilitated comparing the results to the nanoindentation experimental results by Ulm et al. (2007). A random packing of 0.56 was also modeled. To study the feasibility of the DEM models of C-S-H nanostructure, a virtual nanoindentation model was constructed that included a Berkovich indenter represented by rigid elements and particle assemblies to represent the C-S-H specimens. Virtual nanoindentation tests were performed and the force versus displacement curves was extracted from the simulations. The indentation elastic modulus and hardness were then evaluated and compared to the experimental results (Constantinides and Ulm 2007).

2.2 An overview of nanoindentation tests

Figures 2 and 3 show a typical schematic of indentation force/depth curves and the cross section of the indenter. In nanoindentation experiments, the quantities that are related to the mechanical properties of the specimens are indentation hardness and indentation elastic modulus, both of which can be extracted from the indentation force versus indentation depth curves. Based on Ulm et al. (2007), the indentation elastic modulus is calculated as:

$$M = \frac{\sqrt{\pi}}{2}\frac{S}{\sqrt{A_c}} \qquad (1)$$

$$S = \left(\frac{dP}{dh}\right)_{h_{\max}}$$

The indentation elastic modulus M is related to the elastic modulus of the indented material by:

$$M = \frac{E}{1-\nu^2} \qquad (2)$$

where E is the Young's modulus of the indented material, and ν is Poisson's ratio of the indented material. Based on Ulm et al. (2007), the indentation hardness of the specimen is calculated as:

$$H = \frac{P_{\max}}{A_c} \tag{3}$$

where A_c corresponds to the projected contact area. For an ideal Berkovich indenter, A_c is calculated as:

$$A_c = 23.96 \times h_c^2 \tag{4}$$

and h_c is calculated as:

$$h_c = h_{\max} - 0.75(h_{\max} - h_r) \tag{5}$$

$S = (\frac{dP}{dh})_{h_{\max}}$ is calculated by

$$P = b(h - h_p)^m \tag{6}$$

where b and m are parameters fitted from the unloading part of indentation force versus depth. When fracture and cracking occur in the indented material, there is a step in the force-displacement curve. This step is called pop-in. Figure 4 shows a force-displacement curve with a pop-in.

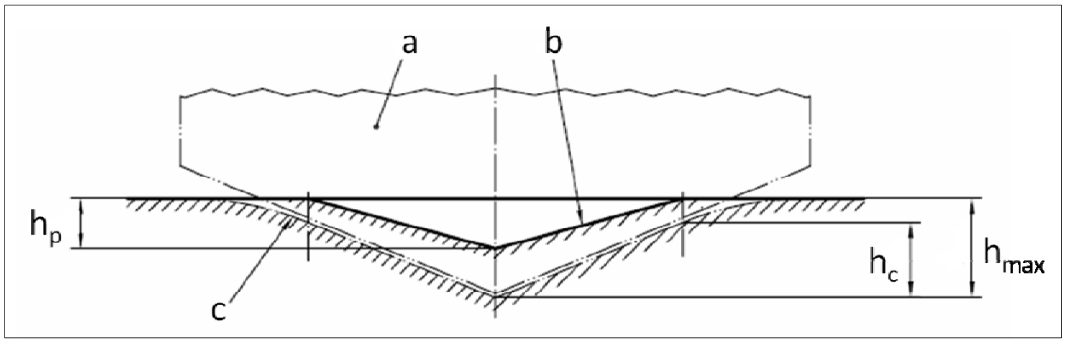

Figure 2. A schematic representation of the cross section of the indenter where "*a*" represents the indenter, "*b*" represents the surface of residual plastic indentation depth in the test specimen, and "*c*" represents the surface of the specimen at maximum depth .

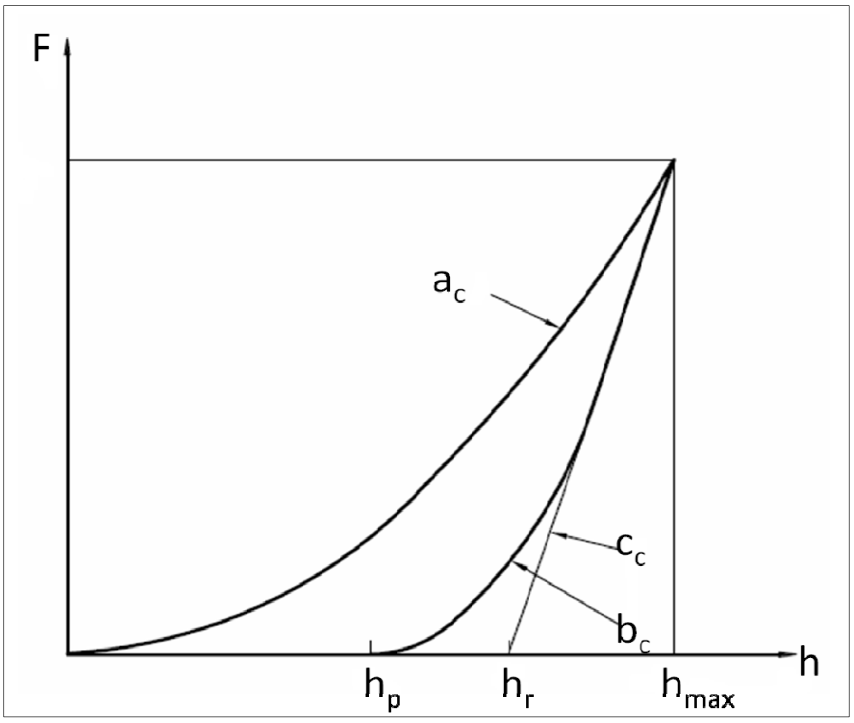

Figure 3. A typical force versus depth indentation curve where "a_c" is the loading curve, "b_c" is the unloading curve, and "c_c" is tangent to curve "b_c" at maximum load.

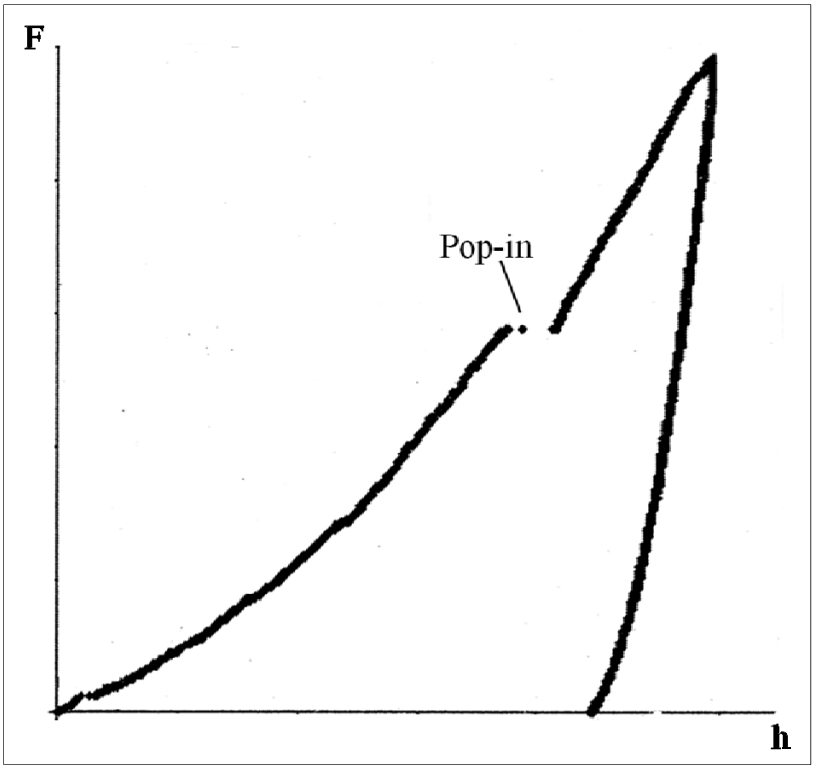

Figure 4. A step, called pop-in, in the force-displacement curve from a nanoindentation test that corresponds to a crack formation in the indented material.

2.3 Nanoindentation tests of C-S-H

Concrete is a composite material with heterogeneities at multiple-length scales. C-S-H is one of the constituents in the composite. Because C-S-H phases are embedded among other phases such as aggregates and calcium hydroxides, special techniques were adopted to perform the nanoindentation tests on C-S-H phases. Mondal et al. (2006) used an Atomic Force Microscope (AFM) to indentify the C-S-H phases and then applied the nanoindenter on the C-S-H phase to develop the load/displacement curves of C-S-H. Figure 5 shows the indentation force/indentation depth of C-S-H in a hardened cement paste sample performed by Mondal et al. (2006). Constantinides et al. (2003, 2007) used a statistical approach to apply large number of indents on the cement paste and then applied a deconvolution algorithm to extract the elastic modulus and hardness of two types of C-S-H phases. Sorelli et al. (2008) also used the statistical nanoindentation test approach to determine the elastic modulus and hardness of C-S-H phases in ultra-high performance concrete. Allison et al. (2011) adopted the statistical nanoindentation test approach to study the elastic modulus and hardness of C-S-H at the impact zone of a dynamically loaded reactive powder concrete panel. Davydov et al. (2011) examined statistical indentation techniques and found that the probed elastic modulus and hardness of C-S-H depended strongly on the indentation depth and that care was needed in choosing the indentation depth.

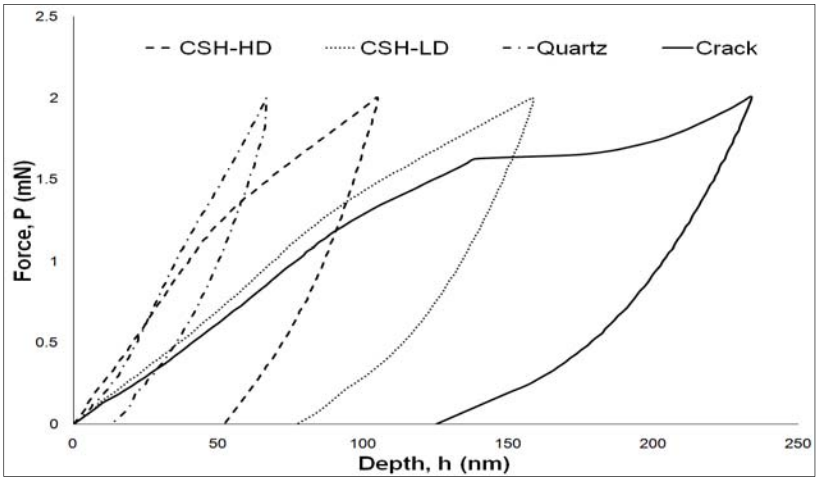

Figure 5. Load displacement curves from nanoindentation tests on C-S-H phases and quartz in hardened cement paste samples.

2.4 Discrete Element Method (DEM)

The DEM models granular materials as individual particles that interact through contact forces. The computation proceeds for each particle by summing the forces and moments at contacts and time integrating Newton's second law to obtain the particle's new location. The problem is highly non-linear, which dictates an explicit form of integration to be used that makes the simulations time consuming for large models. Memory considerations also limit the size of models. In practice, model size is limited to dimensions corresponding to a few hundred thousand particles. Thus, although the DEM is ideal for granular materials, the range of scales that can be explicitly accommodated is small. Generally, the method is used to investigate fundamental material behavior, which is the purpose of the work documented in this report.

In this work, the interactive forces between particles include contact forces, van der Waals forces, and ionic correlation forces. Because the particle size is in the nano-meter range, gravity force is very small relative to these other forces and is ignored. The velocity of each particle is computed from Newton's second law:

$$m_i \frac{\partial v_i}{\partial t} = \sum_{j=1}^{N} F_{nij} + \sum_{j=1}^{N} F_{fij} + \sum_{j=1}^{N} F_{vij} + \sum_{j=1}^{N} F_{eij} \tag{7}$$

where m_i is the mass of particle i, v_i is the velocity of particle i, F_{nij} is the contact normal force applied on particle i by neighboring particle j, F_{fij} is the friction force between particle i and neighboring particle j, F_{vij} is the van der Waals forces between particle i and neighboring particles, j, and F_{eij} is the ionic forces between *particle* i and neighboring particles j. N is the number of contacts.

The rotation of each particle is similarly defined as:

$$I_i \frac{\partial \omega_i}{\partial t} = \sum_{j=1}^{N} F_{fij} r_i + \sum_{j=1}^{N} M_{ij} \tag{8}$$

where I_i is the mass moment of inertia of particle i, ω_i is the rotational velocity of particle i, r_i is the radius of the particle i, and M_{ij} is the rolling

resistance applied on particle i at the contact with an adjacent particle or object j. Note that, although the rolling resistance is small for spherical particles, it is included in the C-S-H model to parametrically account for non-spherical shapes without sacrificing the simplicity of contact detection for ideal spheres.

2.5 Interparticle forces

2.5.1 C-S-H bonding force

2.5.1.1 Introduction

A necessary step in the modeling is the evaluation of the bonding force that provides cohesion for C-S-H and concrete in general. Research results (Gmira et.al 2004, Pellenq et al. 2008) suggest that short- and medium-range surface forces, mediated by partially or totally hydrated calcium ions and with additional contribution of van der Waal's force, provide cohesion for the cement paste. Gmira et al. (2004) also suggest that the short-range surface force might correspond to the cohesion between inter-C-S-H lamellae, and the medium-range surface force might correspond to the cohesion between C-S-H lamella or stacks of lamellae. The medium-range force corresponds to the ionic correlation force. Furthermore, the medium-range surface forces might dominate the short-range surface forces. The medium-range surface force may be calculated by Monte Carlo (MC) simulations using two possible idealizations, i.e., one in which ions are treated as point charges or as charged hard spheres. Using either method, the C-S-H nanoparticle surface is applied with smeared surface charges, and no atomic details are present. A number of studies (Jönsson et al. 2005, Plassard rt al. 2005) showed that the medium-range forces are attractive when there are a large number of divalent ions in the confined solution due to ion-ion correlations, a finding supported by Atomic Force Microscopy (AFM) experiments (Plassard et al. 2005).

The short-range surface force may be calculated by atomistic simulations with atomic details of the surface of C-S-H nanoparticle included. Gmira et al. (1998) performed energy minimization on a Hamid-type Tobermorite-like C-S-H and found that the attractive force is 100 times larger than the medium-range force calculated by Monte Carlo (MC) simulations. Based on a later publication by Pellenq et al. (2008), both short- and medium-

range forces described earlier might be responsible for the bonding of C-S-H.

MC simulations reported in Jönsson et al. 2005 and Plassard et al. 2005 were performed with C-S-H nanoparticle surfaces represented by two flat plates. In the work reported here, the globular morphology was initially assumed, and C-S-H nanoparticles were represented by spheres with diameters of approximately 5 nm, as suggested by Jennings (2000). In the next section in this chapter, an assumption was applied for all medium-range surface forces in the model. In the next chapter, the effects of the bonding force were expanded to include short-range surface forces by increasing the bonding force calculated from MC simulations. In the future, when a more accurate picture of the morphologies of C-S-H nanostructure is obtained, the bonding forces should be calculated based on the distance between individual C-S-H lamellae or stacks of lamellae and the shape of the C-S-H lamellae.

Because of the size of C-S-H nanoparticles, van der Waals forces cannot be ignored. The van der Waals attractive forces are another part of bonding forces and are calculated in this work by using Hamaker's equations for spherical particles.

2.5.1.2 Monte Carlo (MC) simulations of C-S-H medium-range surface forces

The MC simulations of a pair of charged spherical C-S-H nanoparticles were based on Wu and Prausnitz (2002). The simulation box is a 20-nm cube. The charged nanoparticle was represented by hard spheres with a 5-nm diameter and was placed in the diagonal direction in the simulation box. Jonsson et al. (2005) showed that the pore solution of late cement paste had ion concentrations of 20 mM of Ca^{2+} and 40 mM of OH^- and PH levels from 12.5 to 14, which correspond to surface charge densities of approximately 0.16-0.57 C/m^2. Ions were represented by hard spheres with diameters of 0.4 nm (Jonsson et al. 2005). The water was represented by a dielectric constant. The energy in the system included pair potentials between ion species and charges on the nanoparticles, which is given by:

$$\phi(r_{ij}) = \frac{q_i q_j}{4\pi\varepsilon_0\varepsilon_r} \quad \text{if } r_{ij} \geq (d_i + d_j)/2 \tag{9}$$

$$\phi(r_{ij}) = \infty \text{, otherwise}$$

where r_{ij} represents the distance between the center of the ions or nanoparticles, d_i and d_j represent the ion and nanoparticle diameters, respectively, q_i and q_j are the charges of ions and nanoparticles, respectively, ε_0 is the electric permittivity of a vacuum, and ε_r is the relative dielectric permittivity of water. Periodic boundary conditions were applied in the simulation, and the Ewald summation (Ewald 1921) was applied to account for long-range electrostatic interactions. At each separation between two nanoparticles, MC simulations were performed to find equilibrium configurations when energies are minimized. Figure 6 shows a snapshot of C-S-H nanoparticle and ion species at an equilibrium configuration.

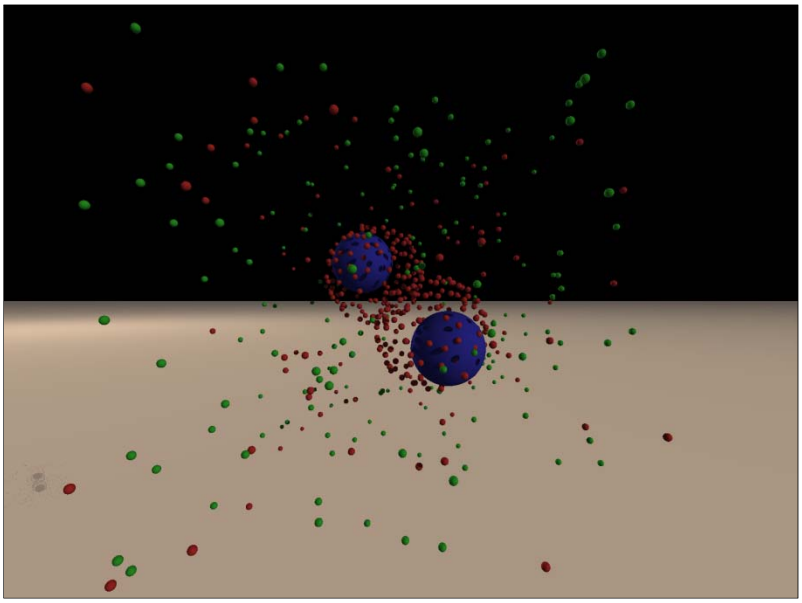

Figure 6. MC simulation result showing that the calcium ions accumulate between negatively-charged C-S-H nanoparticles. The large blue particles represent the C-S-H nanoparticle, small red particles represent the calcium ions, and small green particles represent hydroxyl ions.

After the ion species reach an equilibrium state, the average force between two nanoparticles surrounded by pore solutions is then calculated as:

$$F(r) = -\frac{\partial \phi_{MM}(r)}{\partial r} - \langle \sum_{i=1}^{N} \frac{\partial \phi_{iM}(r_{iM})}{\partial r} \rangle + F^{hs}(r) \quad (10)$$

where ϕ_{MM} represents the pair potential between two nanoparticles, ϕ_{iM} represents the pair potential between nanoparticles and ion species, and $F^{hs}(r)$ represents the average collision force between nanoparticle and ion species. This last term is calculated as:

$$F^{hs}(r) = \lim_{\Delta r \to 0} KT\left(\left(\frac{\langle N_C \rangle}{|\Delta r|}\right)_{\Delta r \langle 0} - \left(\frac{\langle N_C \rangle}{\Delta r}\right)_{\Delta r \rangle 0}\right) \tag{11}$$

where K is Boltzmann's constant, T is absolute temperature, and N_C is the average number of collisions between nanoparticle and ion species with a small variation of distance of nanoparticles, Δr.

Figure 7 shows the average ionic correlation force between two nanoparticles versus gaps between the nanoparticles for different charging densities. The gap between two nanoparticles is the shortest distance between the surfaces of the nanoparticles. The force between nanoparticles due to ion correlations changes from repulsion to attraction with increased surface charging density at a gap of approximately 0.5 nm, which agrees with the experimental results (Plassard et al. 2005).

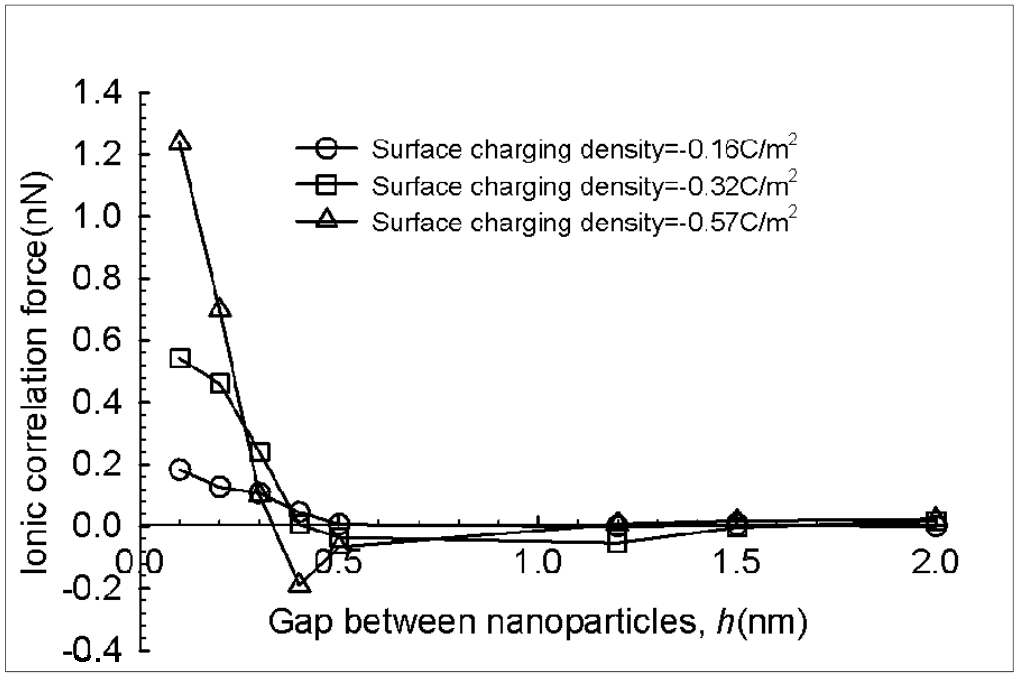

Figure 7. Monte Carlo simulation results showing the average ionic correlation force between two nanoparticles in pore solutions versus the gap between two nanoparticles at different surface charging density.

2.5.1.3 Van der Walls force

Van der Waals forces are attractions between molecules. The energy of interaction between two small particles containing p atoms per cm^3 is given by:

$$E = -\int_{V1} dv_1 \int_{v2} dv_2 \frac{p^2 \lambda}{r^6} \tag{12}$$

where dv_1, dv_2, V_1, and V_2 are volume elements and total volumes of the two particles, r is the distance between dv_1 and dv_2,and λ is the London-Van der Waals constant. Based on Hamaker (1937) for two spherical particles, the energy can be described as:

$$x = \frac{h}{d_1} \quad y = \frac{h}{d_2} \qquad A = \pi^2 p^2 \lambda$$

$$E = -A\frac{1}{12}\left\{\frac{y}{x^2 + xy + x} + \frac{y}{x^2 + xy + x + y} + 2\ln\frac{x^2 + xy + x}{x^2 + xy + x + y}\right\} \tag{13}$$

where h is the shortest distance between the surfaces of two nanoparticles, d_1 and d_2 are the diameters of two nanoparticles, and A is Hamaker's constant.

The van der Waals force between two nanoparticles is then described as:

$$F_v = \frac{\partial E}{\partial h} \tag{13}$$

Based on Jonsson et al. (2005), Hamaker's constant for C-S-H was chosen to be 10^{-20}J. Figure 8 shows the van der Waals force versus gap between a pair of C-S-H nanoparticles.

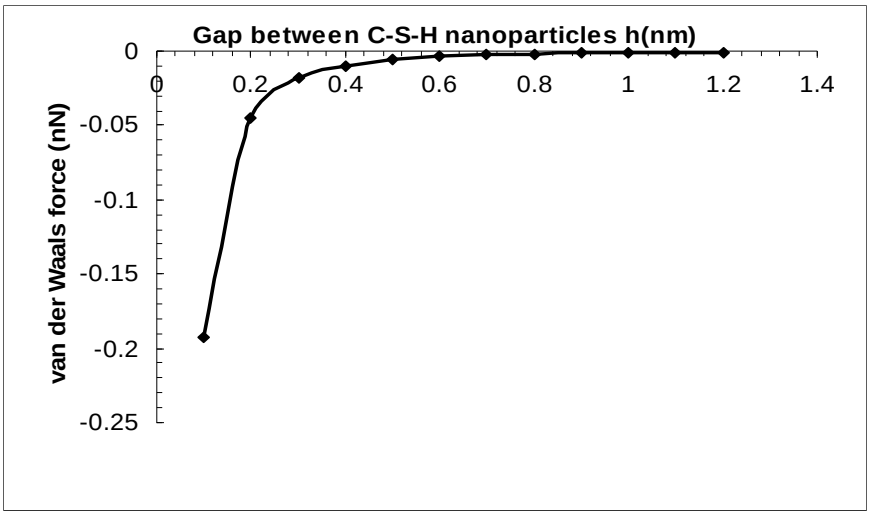

Figure 8. Van der Waals force versus gap between a pair of C-S-H nanoparticles.

2.5.2 Normal contact force

When two particles are in contact, a normal contact force is developed between them. In this work, an elastic Hertzian contact law was used to compute contact forces acting in the direction of the contact normal vector. Figure 9 shows the schematic of two spheres in contact.

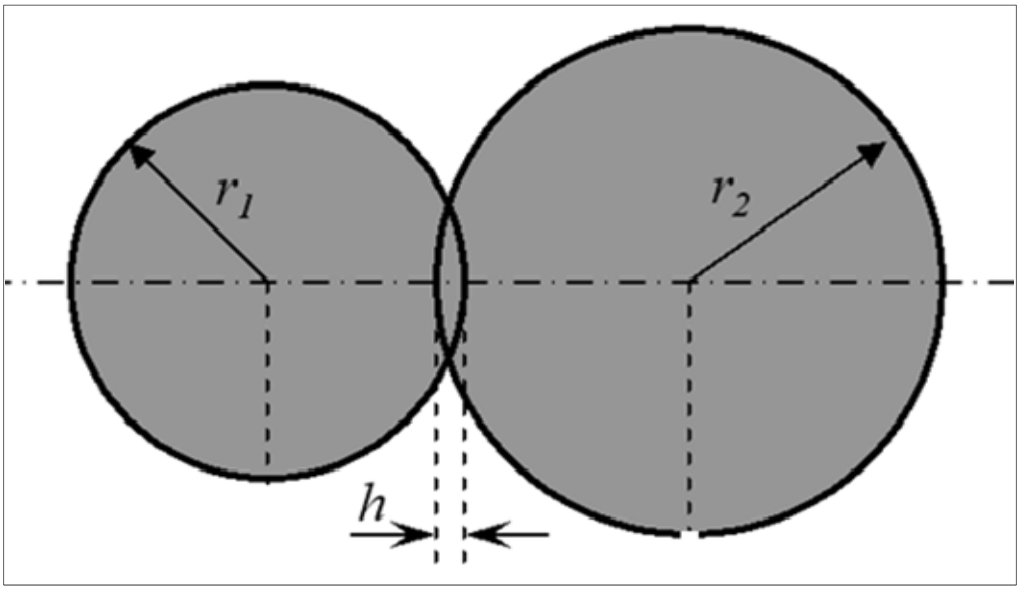

Figure 9. A schematic of two spheres in contact.

The normal contact force is defined as:

$$F_n = \frac{4E_c r_c^{1/2} h^{3/2}}{3} \tag{14}$$

where h is the penetration of the spheres in contact, and r_c is the equivalent radius defined as:

$$r_c = \frac{r_1 r_2}{r_1 + r_2} \tag{15}$$

where r_1 and r_2 represent the radius of the respective contact particles. E_c is the equivalent Young's modulus defined as:

$$E_c = \left(\frac{1-\nu_1^2}{E_1} + \frac{1-\nu_2^2}{E_2}\right)^{-1} \tag{16}$$

where E_1 and E_2 are the elastic modulus of each contact particle, and ν_1 and ν_2 are the Poisson's ratio of each contact particle. In this model, all the particles have the same elastic modulus and Poisson's ratio.

2.5.3 Net normal force

The interparticle forces are very complex at the nano-meter range. According to Feiler et al. (2000) at short ranges (less than 0.5 nm), the Born repulsion takes effect, which is the origin of the mechanical contact force. In this work, it was assumed that the mechanical contact force takes effect when the gap between two nano-particles was within 0.45 nm, which is slightly larger than the ion diameter. Within this range, the mechanical contact force dominates, and the van der Waals force and ionic force are set to remain constant. When the gap between nano-particles exceeds 0.45 nm, the net force becomes attractive, and ionic attractive forces dominate. Based on the calculation results and equations from previous sections, the individual forces and net forces versus distance between two particles are calculated and plotted in Figure 10.

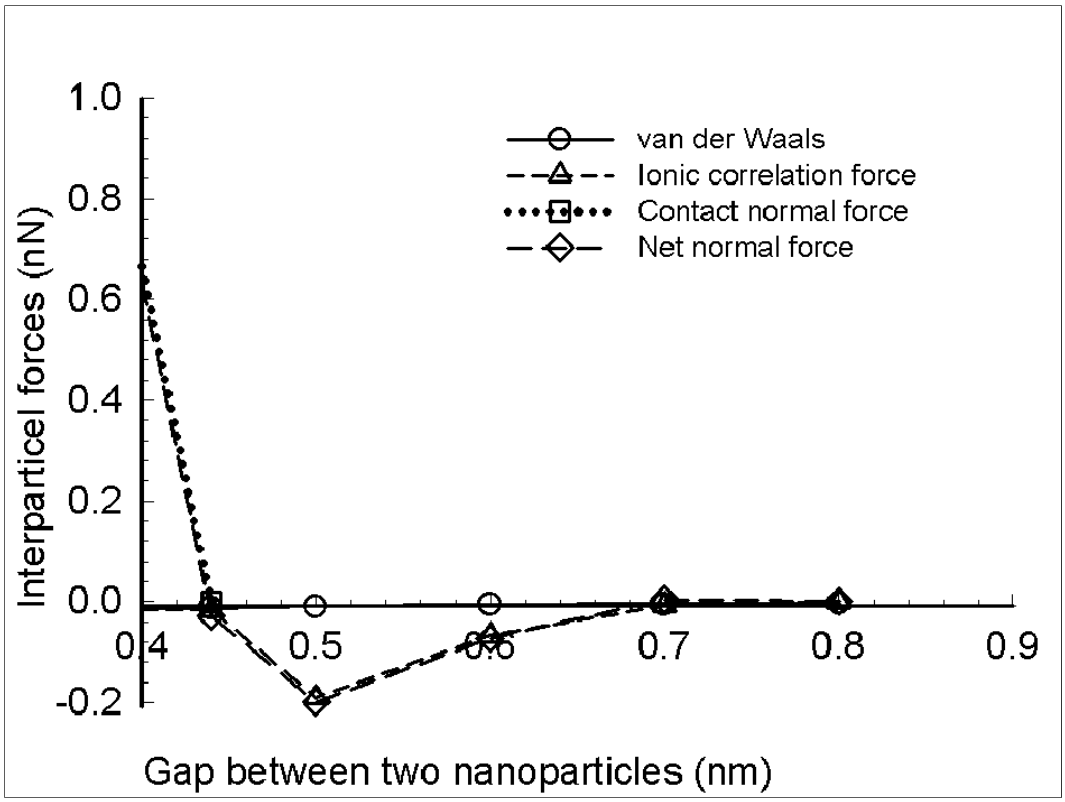

Figure 10. The normal interparticle forces versus gap between two nanoparticles.

Figure 11 shows that the van der Waals attractive force is much smaller than the ionic attractive force; thus the ionic attractive force is responsible for the cohesion. Figure 11 also shows that the equilibrium position of the particles is about 0.44 nm. When the gap between nano-particles is smaller than this value, the net force is repulsive, and mechanical contact force and friction force dominate. When the gap between nano-particles exceeds this value, the net force becomes attractive, and ionic attractive forces dominate.

2.5.4 Tangential contact force

Tangential contact forces occur between C-S-H nanoparticles. The tangential contact force is defined at time t_{i+1} as:

$$F_{f\,i+1} = F_{f_i} + K\ \Delta \mathbf{v}_t\ \Delta t \tag{17}$$

where $\Delta \mathbf{v}_t$ is the relative velocity of the two objects at the contact point in the plane perpendicular to the normal contact direction, K is a stiffness constant set in the tangential direction, and Δt is the time interval. The

absolute value of the tangential force is limited by the maximum friction $F_{\max}$ force defined as:

$$F_{f\max} = F_n f_s \tag{18}$$

where f_s is the friction factor. The friction factor is equal to either the static friction factor f_s if no sliding occurs or the dynamic friction factor f_d if sliding occurs. Sliding is activated when the force predictor first exceeds $F_n f_s$. Sliding continues when the force predictor remains greater than $F_n f_d$. Sliding stops when the force predictor becomes smaller than $F_n f_d$. In our simulations, the dynamic friction factor is slightly lower than the static friction factor.

2.5.5 Rolling contact resistance

Rolling contact resistance is used to include the effects of non-spherical shapes for objects that are simulated using perfectly spherical particles. The rolling resistance moment is defined as:

$$M_{i+1} = M_i + K_M \Delta\boldsymbol{\omega}_r \Delta t \tag{19}$$

The parameter K_M is a rotational stiffness. The rolling resistance M_{i+1} cannot exceed a maximum value defined by:

$$M_{\max} = F_n d f_R \tag{20}$$

where F_n is the normal contact force, d is the distance between the centers of the two particles in contact, and f_R is a "friction" coefficient for rolling. At variance to the other forces acting at contacts, rolling resistance is difficult to quantify because it is not an intrinsic property of the material but rather a device to capture the effect of particle shape. In this paper, the rolling resistance was used to investigate the importance of particle rotation to the overall nano-indention resistance. Initially, a small rotational stiffness of 1e-4 nN.nm/rad was used to model spherical particles.

2.6 Particle generation

C-S-H nanostructure formation involves nucleation and growth of C-S-H nano-particles. A complex model accounting for the detailed chemical, physical, and atomic process of hydration is required to generate C-S-H nanostructure realistically. This type of model has not yet been developed. Alternatively, in this study, we generated three packing arrangements to represent C-S-H nanostructures whereby the arrangements were controlled to have specified packing ratios. Packing ratio is defined as the volume fraction of the particles in the simulation domain. The cases considered were random loose packing (packing ratio ≈ 0.56), random close packing (packing ratio ≈ 0.64), and dense close packing (packing ratio$=0.74$). The last two packing arrangements correspond to low-density C-S-H and high-density C-S-H, respectively. Generating dense close packing is straightforward. To generate random packing, we began by placing a cluster of four nano-particles as a nucleus in the middle of a controlled volume. Particles were added one-by-one with each particle touching at least three existing particles to form a stable configuration until the particles filled the volume. After the particles were generated, the inter-particle forces were activated, and dynamic equilibration was performed until the energy of the system was minimized. The resulting configuration was the final particle configuration before external loads were applied. Figure 11 shows three final particle arrangements. The specimen size is 700 nm by 700 nm by 150nm.

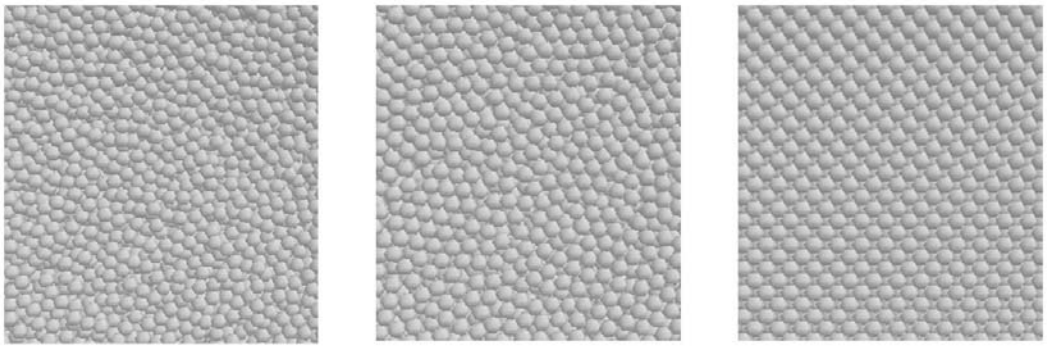

(a) (b) (c)

Figure 11. The particle arrangements for three packing ratios i.e., (a) random packing (packing ratio ≈ 0.56), (b) random packing (packing ratio ≈ 0.64), and (c) close dense packing (packing ratio=0.74).

2.7 DEM model set up and parameters

A Berkovich indenter was numerically constructed as a rigid element, which is a reasonable assumption because the indenter is much stiffer than the C-S-H specimens. The radius of the indenter tip was set to be 5 nm. The tip radius of a realistic nano-indenter normally ranges from 50 nm to 100 nm, and indentation depth is more than 250 nm. In this study, the indentation depth of the DEM simulations was set to be 25 nm because of computer resource limitations. Therefore, a tip radius of 5 nm was used to minimize the effects of the tip geometry on the indentation modulus and hardness.

Figure 12 shows a C-S-H nano-particle assembly and a Berkovich nano-indenter. The particle assembly was fixed in all directions on the bottom and fixed in the two horizontal directions on the sides of the domain. The virtual indentation was displacement-controlled with a travel speed of 1 nm/ns. When the indentation depth reached 25 nm, the indenter was retracted completely at the same speed.

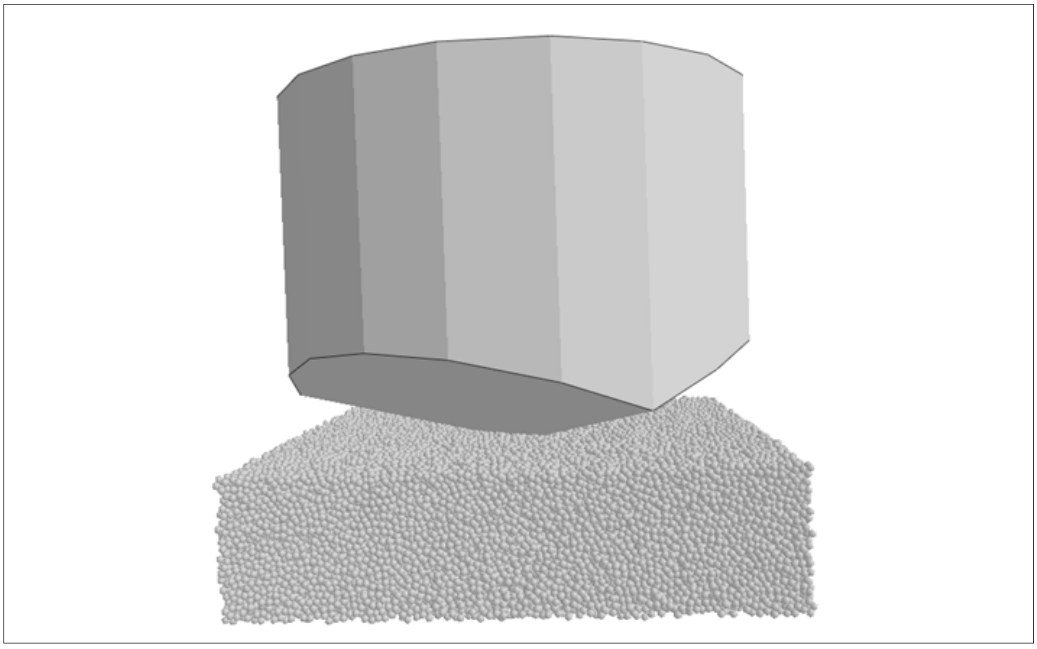

Figure12. The C-S-H nanoparticle assembly and the Berkovich indenter in DEM simulations.

The parameters used in the DEM simulations are summarized in Table 1.

Table 1. Parameters used in the initial DEM simulations.

Input parameters	Values
Diameter of the particles	5 nm (Jennings 2004)
Density of the particles	2604 Kg/m3 (Allen et al. 2007)
Elastic modulus of the particles (*E*)	57 GPa (Constantinides et al. 2007)
Hamaker's constant	*A*=1.6e-20 Joule (Andandarajah and Chen 1997)
Static friction between particles	0.8 (Feiler et al. 2000)
Dynamic friction between particles	0.7
Static friction between indenter and particles	0.3
Dynamic friction between indenter and particles	0.2
Rotational stiffness	1e-4 nN.nm/rad
Electric charging density on the surface of C-S-H gel	0.57 C/m^2 (Jonsson et al. 2000)
Gap for initial contact	0.45 nm (Feiler et al. 2000)
Gap threshold for van der Waals force	0.45 nm (Feiler et al. 2000)

2.8 Results and discussion

Figure 13 shows the indentation force versus indentation depth for three packing ratios. The indentation force increases with increased packing ratio. For the specimens with packing ratios of 0.56 and 0.64, force-displacement curves and indentation snapshots show plastic deformation during the indentation process. After unloading, there are residual pyramid-shaped imprints in the specimens, as shown in Figure 13. For the specimens with a packing ratio of 0.74, the force-displacement curve is much steeper than the other two packing ratios, and a force drop occurs at the indentation depth of 17 nm that corresponds to crack formation in the specimen. After the crack forms, the indentation force flattens while more cracks grow, and then drops again as clusters of particles crack apart. After unloading, there is a residual imprint, and cracked particle clusters are evident. The corresponding snapshots in Figure 13 show the crack formation, growth, and cracked particle clusters.

In Figure 13, the load-displacement curves for packing ratios of 0.56 and 0.64 can be used to calculate the indentation hardness. However, the load-displacement curve for a packing ratio of 0.74 cannot be used because fracture occurred during the indentation. Table 2 shows the indentation modulus and hardness calculated from the data in Figure 13 and the experimental data from Constantinides and Ulm (2007). Table 2 shows that the indentation modulus calculated from DEM simulations is only about half of the experimental data, and the indentation hardness from DEM is almost one order of magnitude smaller than the experimental data for a packing ratio of 0.64.

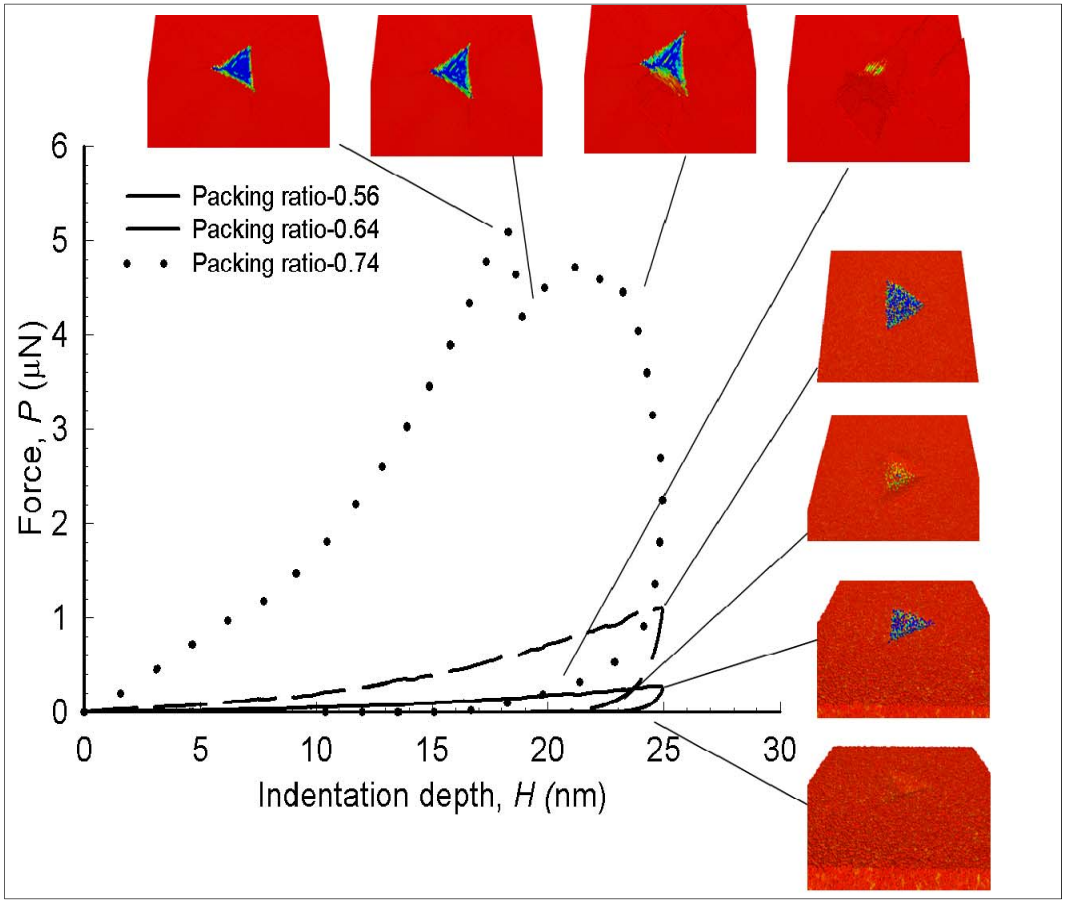

Figure 13. The indentation force versus indentation depth for specimens with packing ratios of 0.56, 0.64 and 0.74. The snap shots show the progression of indented particle assembly. The color shows the stresses in the vertical direction of the specimen.

Table 2. The indentation modulus and indentation hardness calculated from DEM results in Figure 14 and experimental results from Constantinides and Ulm, 2007, and Ulm et al. 2007).

	Indentation modulus *M* (GPa)		Indentation hardness *H* (GPa)	
0.56	DEM	Exp (Constantinides and Ulm, 2007; and Ulm, et al. 2007)	DEM	Exp (Constantinides and Ulm, 2007; Ulm, et al. 2007)
	1.7	≈ 8.7	0.02	≈ 0.19
0.64	5	18.2 ± 4.2	0.086	0.44 ± 0.14

3 Parametric Studies

3.1 Introduction

Nanoindentation simulations in the previous chapter showed that both elastic modulus and hardness of a C-S-H matrix from simulations are smaller than the experimental data (Constantinides and Ulm 2007). In this chapter, we investigated the possible reasons for this difference by performing parametric studies on different parameters that might affect the properties of the C-S-H matrix. Those studies also helped us look into the possible nature of interparticle forces and also provided insight into possible ways to improve the properties of the C-S-H matrix.

3.2 Effects of rotational stiffness

As described previously, rotational resistance is applied in the models to account for the non-spherity of the C-S-H nano-particle. Figure 14 shows indentation force versus indentation depth with different applied rotational stiffnesses for packing densities of 0.56, 0.64 and 0.74. Figures 14(a and b) show that, for packing densities of 0.56 and 0.64, indentation forces increase with increased rotational resistance, although force/depth curves for these packing densities are all similar with mostly plastic deformation and small elastic recovery. For a packing density of 0.74, the force/depth curves and snapshots of the C-S-H nano-particle assembly under indentation force in Figure 14(c) show that the force/depth curves follow the similar trend until the indentation depth reached about 17 nm. When indented further, the specimen cracks under the indentation force when rotational resistance is almost zero and small (rotational stiffness=1 nN.nm/rad), and the specimen doesn't crack when rotational resistance is sufficiently high (rotational stiffness > 10 nN.nm/rad). The force/depth curves for rotational stiffnesses higher than10 nN.nm/rad show little plasticity and the elastic recovery is large, and three curves with rotational stiffnesses higher than 10 nm.nN/rad almost overlap each other. It appears that for a packing density of 0.74, sufficient rotational resistance can prevent the specimen from cracking. However when the specimen does not crack, increasing rotational resistance further has little effects on the response of the specimen.

The elastic modulus of a C-S-H matrix is calculated from the force/depth curves in Figure 15 and Equations 1-6 and is plotted in Figure 15, which shows that the elastic modulus of C-S-H matrix increases drastically as rotational stiffness is increased from 1e-4 to 1 nN.nm/rad. Above 1 nN.nm/rad, a much smaller increase occurs in the computed elastic modulus. Figure 15 also shows that for packing densities of 0.56 and 0.64 and with rotational stiffness greater than 1e-4 nN.nm/rad, the elastic modulus of the C-S-H matrix computed from simulations agree well with values computed from the experiments. For a packing density of 0.74, the elastic modulus of a C-S-H matrix computed from simulations are slightly higher than the range from the experiments for the C-S-H matrix with comparable packing density when rotational stiffness is greater than 10 nN.nm/rad. Note that elastic modulus was not extracted from force/depth curves in Figure 14(c) for a rotational stiffness of 1e-4 and 1 nN.nm/rad because cracks formed prior to the unload phase of the simulation.

Figure 16 shows the hardness of the C-S-H matrix versus the rotational stiffness. The hardness for different applied rotational stiffnesses and packing densities are calculated based on the force/depth curves in Figure 14. The experimental data from Constantinides and Ulm (2007) are also plotted for comparison. Figure 16 shows that the hardness of C-S-H matrix from simulations increases drastically when the rotational stiffness increases from 1e-4 to 1 nN.nm/rad for packing densities of 0.56 and 0.64. However, little increase in hardness occurs when the rotational stiffness increases further. Moreover, for rotational stiffnesses greater than 10 nN.nm/rad, the hardness of C-S-H matrix from simulations agrees well with experimental data for comparable packing densities.

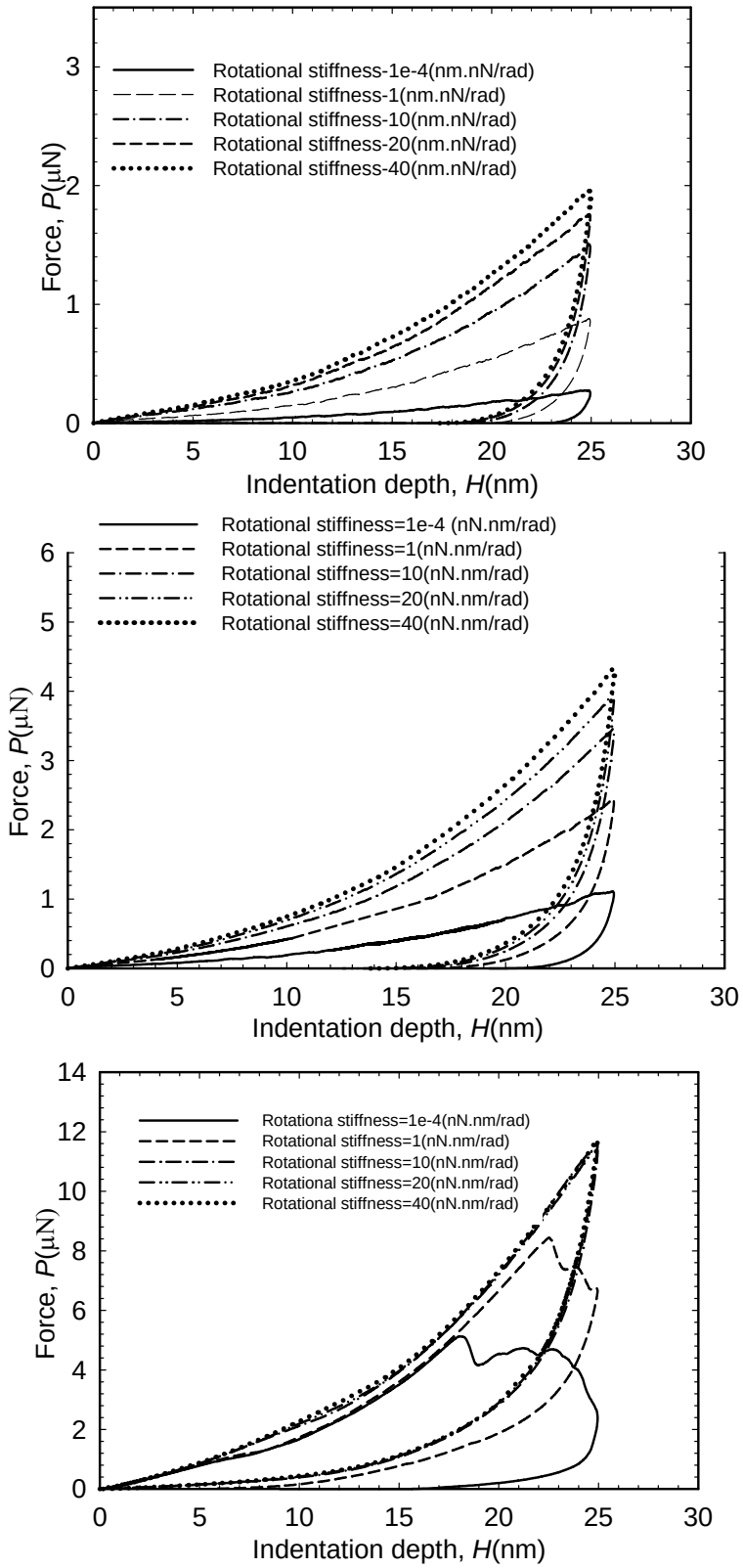

Figure 14. Indentation force versus indentation depth for different rotational stiffness while other parameters stay constant for (a) Packing ratio of 0.56, (b) Packing ratio of 0.64, and (c) packing ratio=0.74.

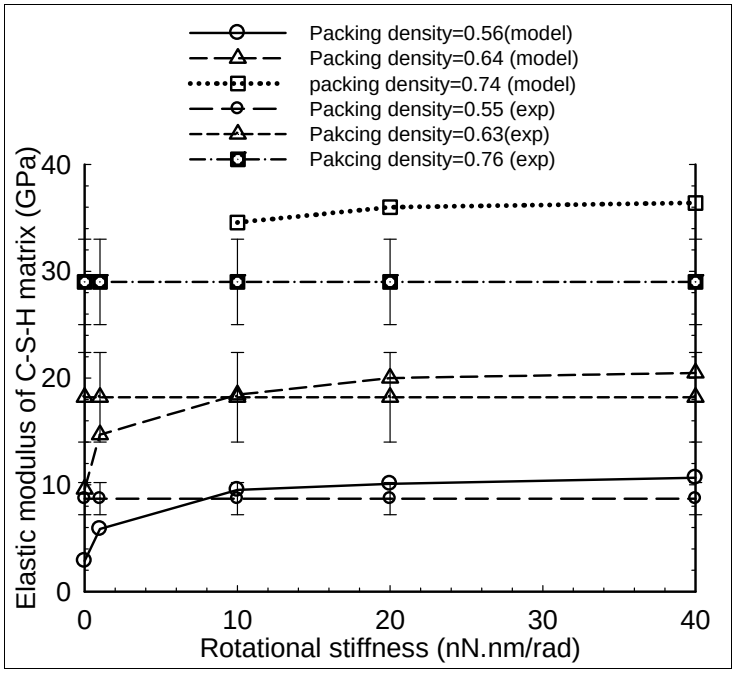

Figure 15. Elastic modulus of C-S-H matrix from simulations increases drastically when the rotational stiffness is increased from 1e-4 to 1 nN.nm/rad for packing densities of 0.56 and 0.64. However, little increase occurs when the rotational stiffness is increased further.

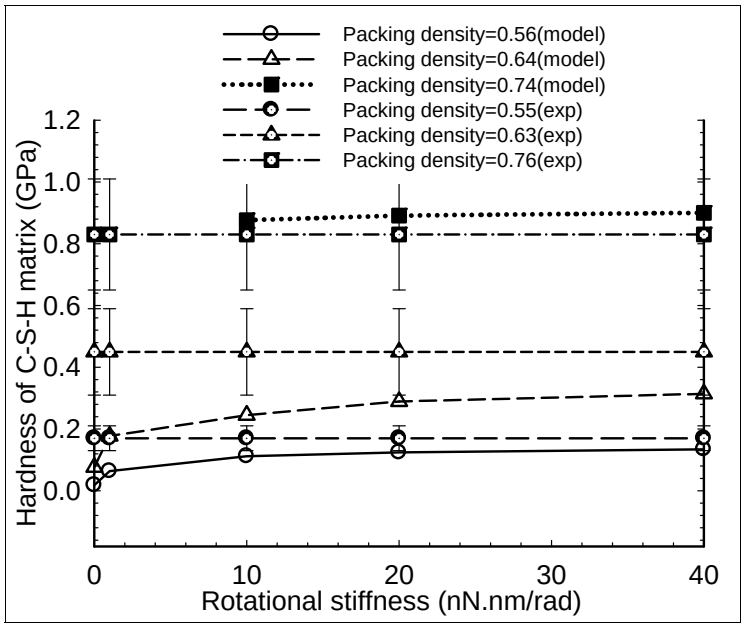

Figure16. The hardness of C-S-H matrix from simulations increases drastically when the rotational stiffness increases from 1e-4 to 1 nN.nm/rad for packing densities of 0.56 and 065 while little increase in hardness is seen when the rotational stiffness is increased further.

3.3 Effects of normal cohesive force

Research from Gmira et al. 2004 and Pellenq et al. 2008 suggests that short-and medium-range surface forces, mediated by partially or totally hydrated calcium ions and with the additional contribution of van der Waal's force, provide cohesion for the cement paste. In our MC simulations, we only considered van der Waals forces and the ionic correlation force that is medium-range surface forces. To explore the possible bonding mechanisms between C-S-H nano-particles, the possibility was considered of an inter-particle normal cohesive force that is in addition to van der Waals forces and ionic correlation forces by varying the maximal normal cohesive force between nano-particles. The maximal normal cohesive force will be simply referred to as the normal cohesive force in the remainder of this paper. All other parameters are the same as listed in Table 1.

Figure 17 shows the indentation force P versus indentation depth H with various normal cohesive forces for a packing ratio of (a) 0.56, (b) 0.64, and (c) 0.74. For packing ratios of 0.56 and 0.64, Figures 17(a and b) show that increased normal cohesive force leads to steeper force versus depth curves along with higher forces at the maximal depths. For a packing ratio of 0.74 when the maximal normal cohesive force is doubled to 0.38, the specimen did not crack but also displayed little plasticity. The indention curves become steeper with increased normal cohesive force.

The elastic modulus of C-S-H matrix that was estimated from the force/depth curves in Figure 17 is plotted in Figure 19. The experimental data from Constantinides and Ulm (2007) are also plotted for comparison. Figure 18 shows that the elastic modulus of C-S-H matrix increases with increased normal cohesive force. The increase in elastic modulus is steeper when the normal cohesive force doubled to 0.38 nN and becomes less steep when the cohesive force increases further. Figure 18 shows that the increase in elastic modulus is higher for higher packing densities and that the elastic modulus of C-S-H matrix from the simulations agrees with experimental data for packing densities of 0.56 and 0.64 and is higher than the experimental data for a packing density of 0.74 when the normal cohesive force is doubled to 0.38 nN from the ionic correlation force estimated from Monte Carlo simulations.

The hardness of C-S-H matrix was also estimated from the indention curves in Figure 17 and is plotted in Figure 19. The experimental data from

Constantinides and Ulm (2007) are also plotted for comparison. Figure 19 shows that the hardness of C-S-H matrix increases with increased maximal normal cohesive force. The increase in hardness is steeper when the normal maximal cohesive force is doubled to 0.38 nN and become less steep when the maximal normal cohesive force increases further. Figure 19 shows that the increase in hardness of C-S-H matrix is higher for higher packing densities and that the hardness of C-S-H matrix from simulations is lower than the experimental data for packing densities of 0.56 and 0.64 and slightly higher than the experimental data for a packing density of 0.74. However, the magnitude of hardness approaches the experimental data when the normal cohesive force is less than 10 times of the ionic correlation force estimated from Monte Carlo simulations, which is much smaller than the two order of magnitude increase of ionic covalent bonding force estimated by atomistic simulations (Pellenq et al. 2008).

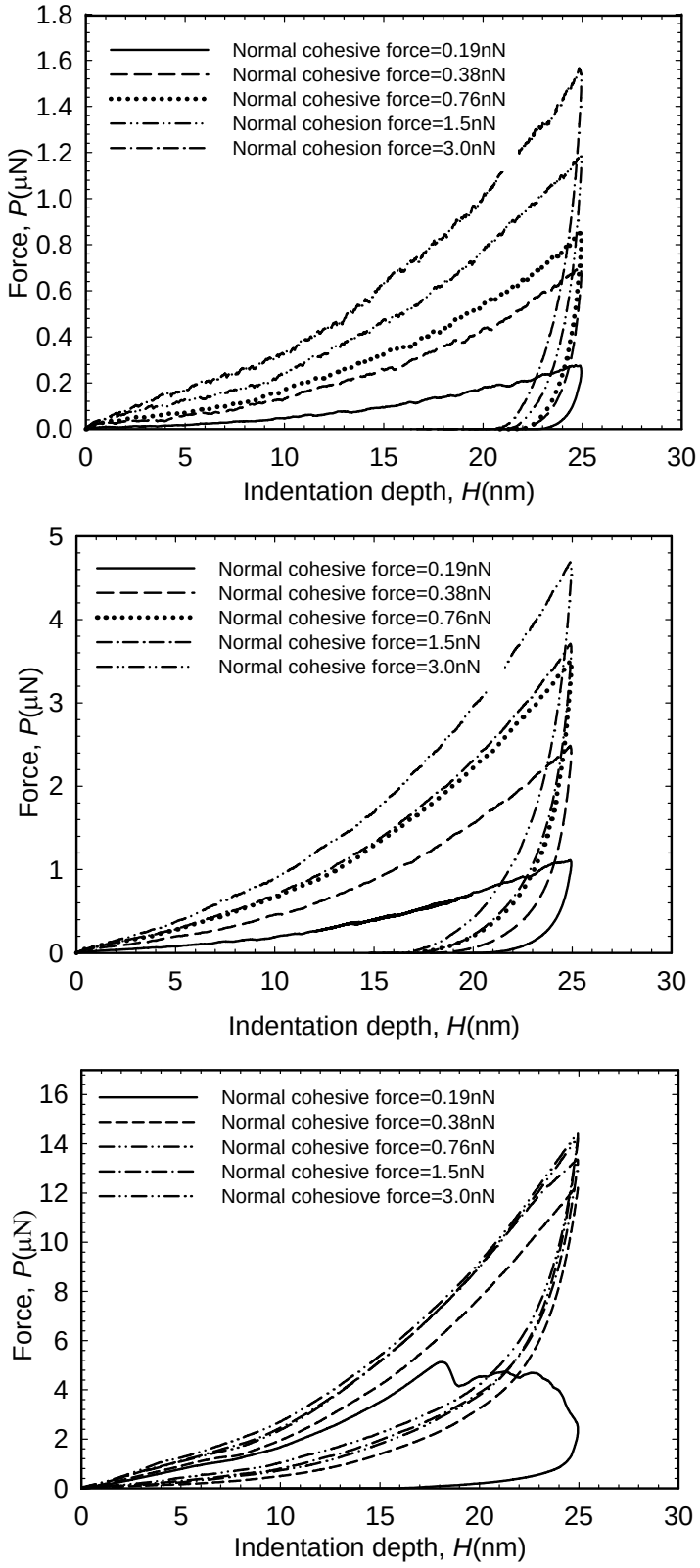

Figure 17. Indentation force versus indentation depth for various normal cohesive forces, keeping other parameters as they are listed in Table 1 for (a) Packing ratio=0.56, (b) Packing ratio=0.64, and (c) packing ratio=0.74.

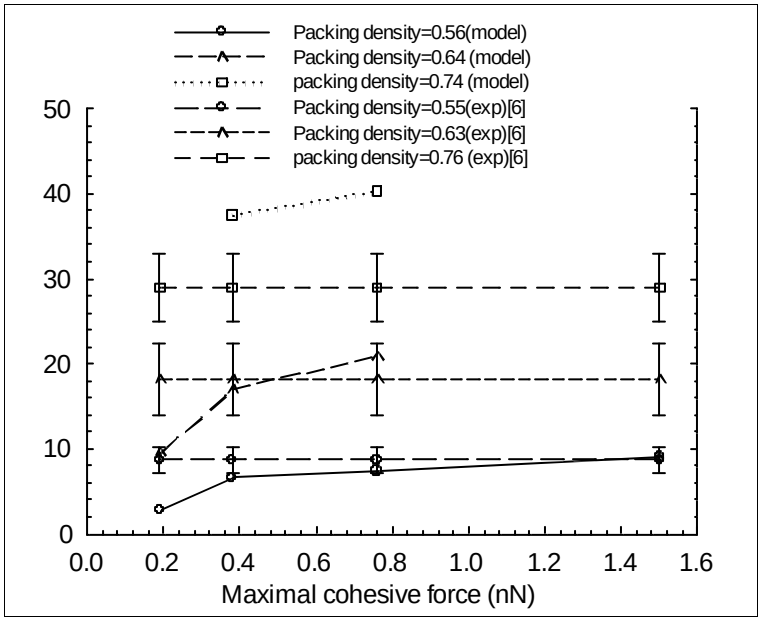

Figure 18. Elastic modulus of C-S-H matrix estimated from the data in Figure 17.

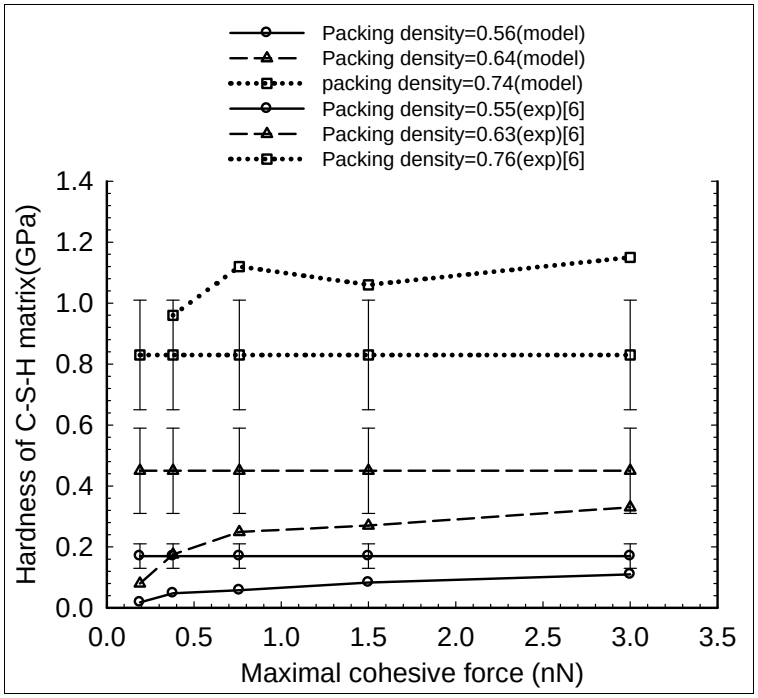

Figure 19. Hardness of C-S-H matrix estimated from the data in Figure 17.

3.4 Effects of sliding friction coefficient

As described in section 2.5.4, the tangential force is limited by the sliding friction coefficient, which is supported by the fact that the strength of cement-based materials is pressure-dependent. In this study, we varied

the sliding friction coefficient to study the effects of sliding friction coefficient on the properties of C-S-H matrix.

Figures 20 (a and b) show that, for packing densities of 0.56 and 0.64, the force/depth curves become steeper with increased sliding friction coefficient, and the indentation force at maximum indentation depth is higher. Figure 20 (c) shows that the force/depth becomes steeper with increased sliding friction coefficient, but all three curves suggest crack formation during indentation process.

The elastic modulus of C-S-H matrix estimated from the force/depth curves in Figures 20 (a and b) is plotted in Figure 21. Figure 21 shows that the elastic modulus of C-S-H increases with increased sliding friction coefficient, and the increase is higher for higher packing densities. Figure 21 also shows that, with little rotational resistance and ionic correlation force from Monte Carlo simulations, the elastic modulus of C-S-H matrix from simulations with very high sliding friction coefficients are still lower than the experimental results from Constantinides and Ulm (2007). Evidently, either higher rotational resistance or higher cohesive normal force, or both, are required in the model to produce the observed stiffness of the C-S-H matrix for the comparable packing densities. Increasing sliding friction coefficient also makes the C-S-H matrix stiffer.

The hardness of C-S-H matrix estimated from force/depth curves in Figure 20 (a and b) is plotted in Figure 22. Figure 22 shows that the hardness of C-S-H matrix increases with increased sliding friction coefficient. The increase is higher for higher packing density. Figure 22 also show that the hardness from simulations is much lower than the experimental data (Constantinides and Ulm 2007), for both packing densities of 0.56 and 0.64, which also indicates that higher rotational resistance or higher normal cohesive force is required in the model to produce the strength of C-S-H matrix from experimental results.

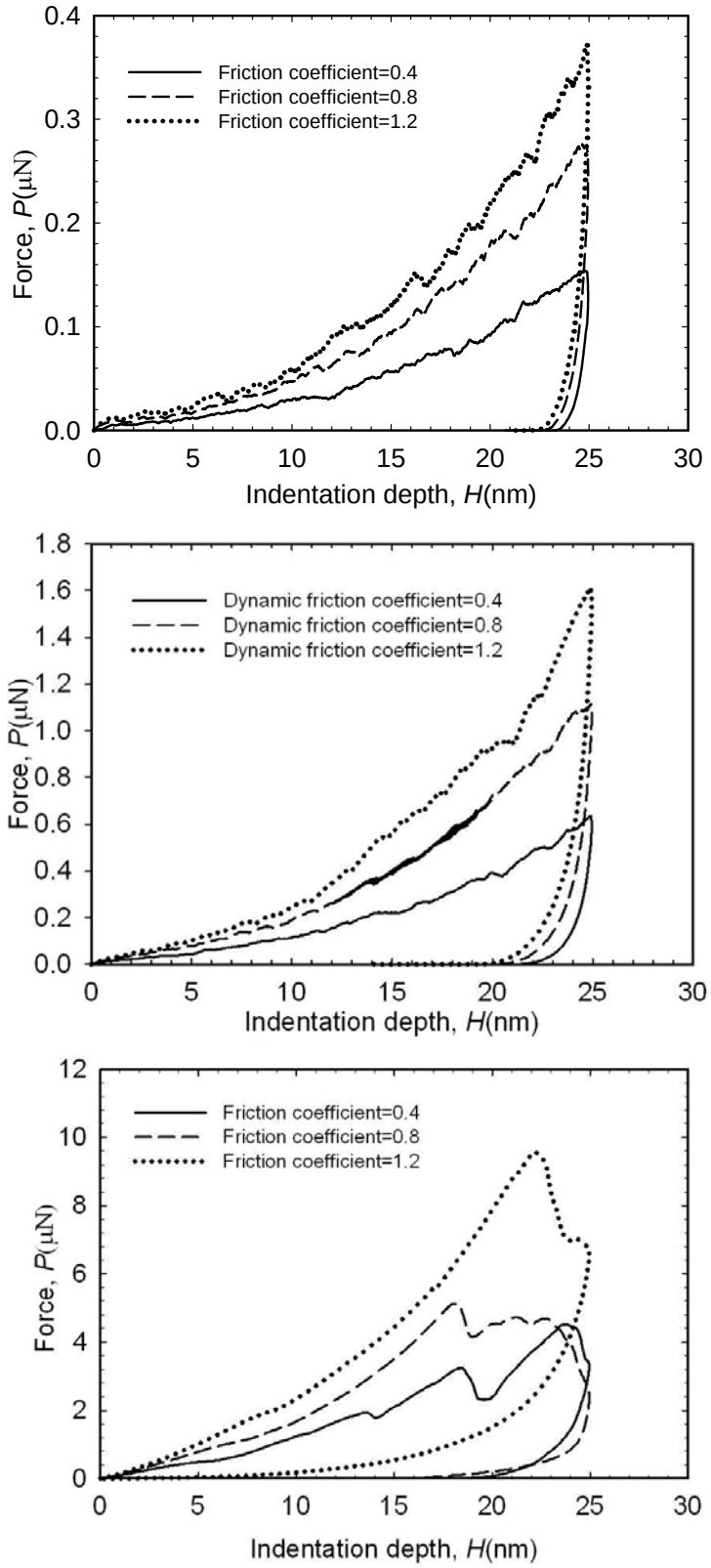

Figure 20. Indentation force versus indentation depth for different values of sliding friction coefficient, while other parameters stay the same as that listed in Table 1, for (a) Packing ratio=0.56, (b) Packing ratio=0.64, and (c) packing ratio=0.74.

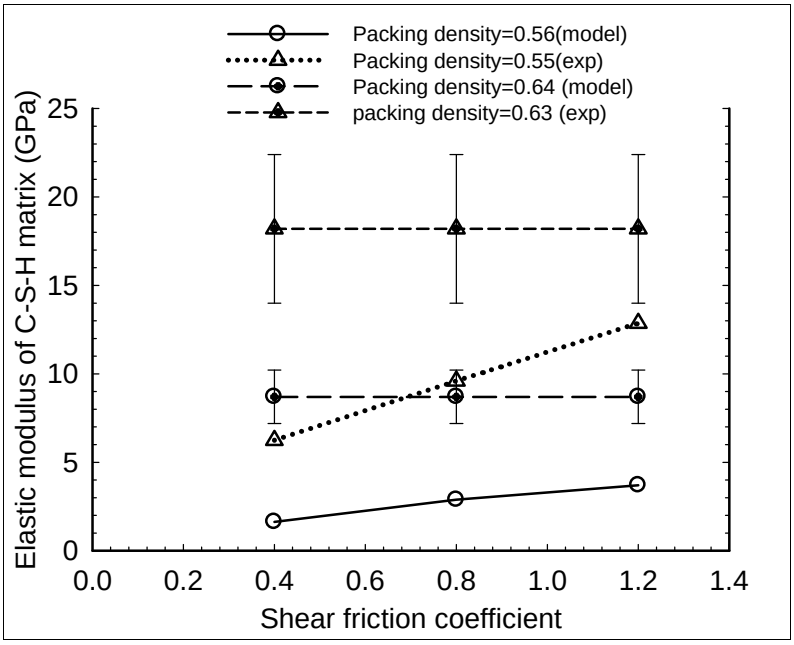

Figure 21. Elastic modulus of C-S-H matrix estimated from the data in Figure 20.

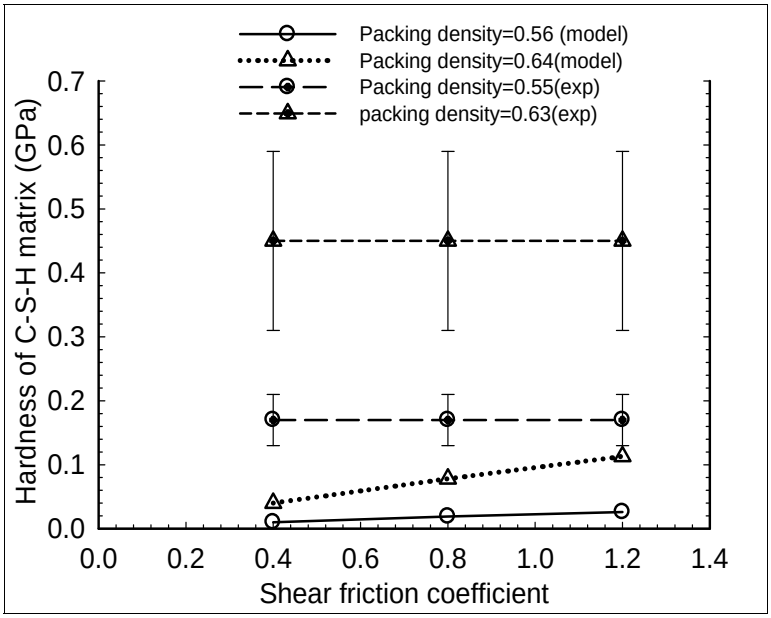

Figure 22. Hardness of C-S-H matrix estimated from the data in Figure 20.

3.5 Effects of elastic properties of C-S-H nanoparticles

Pellenq et al. (2008) studied the elastic properties of C-S-H nano-particles by using atomistic simulations and found the estimated elastic modulus to be about 57 GPa. Other researchers (Manzano , et. al,2009) got similar results.

The sensitivity analysis for particle elastic properties evaluated the effect of elastic properties of individual C-S-H nano-particles on the properties of the C-S-H matrix. The analysis used the value of 57 GPa given in Table 1 by considering two higher values (89 GPa and 160 GPa) for the elastic modulus of C-S-H nano-particles. In these sets of simulations, the other parameters in Table 1 remained unchanged. Figure 23 shows that the indentation force/ indentation depth curves are very close for packing densities of 0.56 and 0.64, and that the force/depth curves follow each other until cracks form for a packing density of 0.74. The maximum force is higher with increased particle elastic modulus.

The elastic modulus of C-S-H matrix estimated from force/depth curves in Figures 23 (a and b) is plotted in Figure 24. Figure 24 shows that the elastic modulus of C-S-H matrix is almost unchanged with increased particle elastic modulus for a packing density of 0.56, although it increases with increased particle elastic modulus for a packing density of 0.64.

The hardness of C-S-H matrix estimated from Figure 23 is plotted in Figure 25. Figure 25 shows that the hardness of C-S-H matrix is almost unchanged with increased particle elastic modulus.

Figures 24 and 25 indicate that the C-S-H matrix is stiffer but not stronger if the particle elastic modulus is increased.

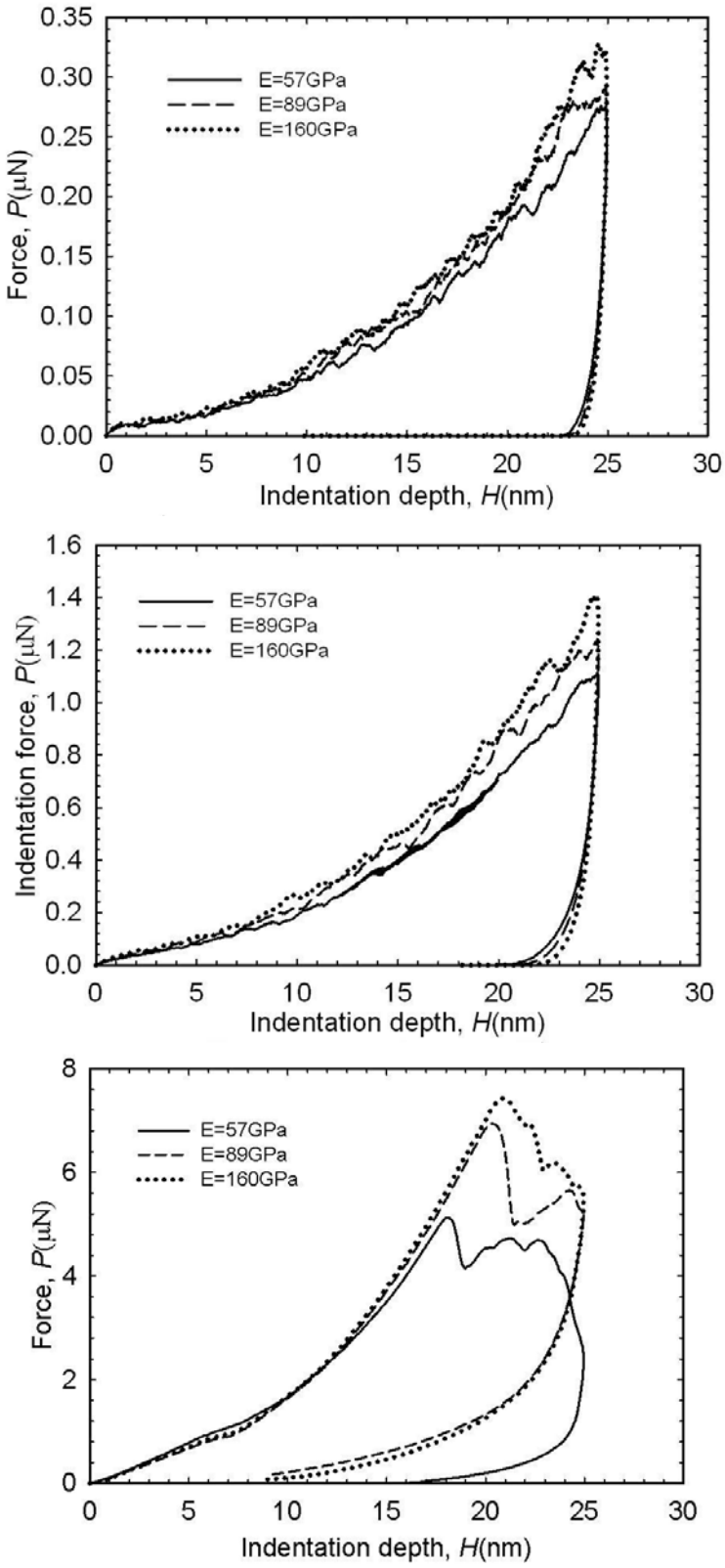

Figure 23. Indentation force versus indentation depth for different particle elastic moduli, while other parameters stay the same as that listed in Table 1, for (a) Packing ratio=0.56 (b) Packing ratio=0.64, and (c) packing ratio=0.74.

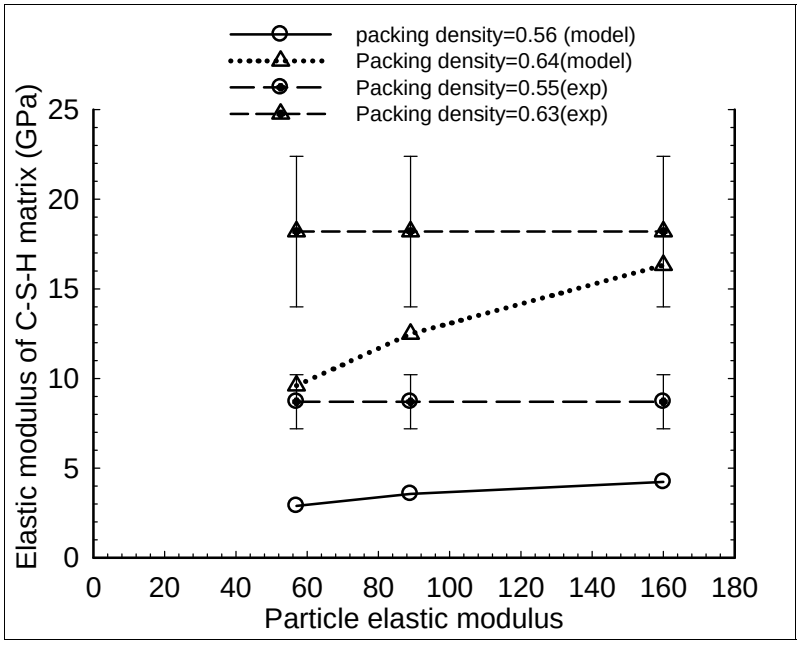

Figure 24. Elastic modulus of C-S-H matrix estimated from the data in Figure 23.

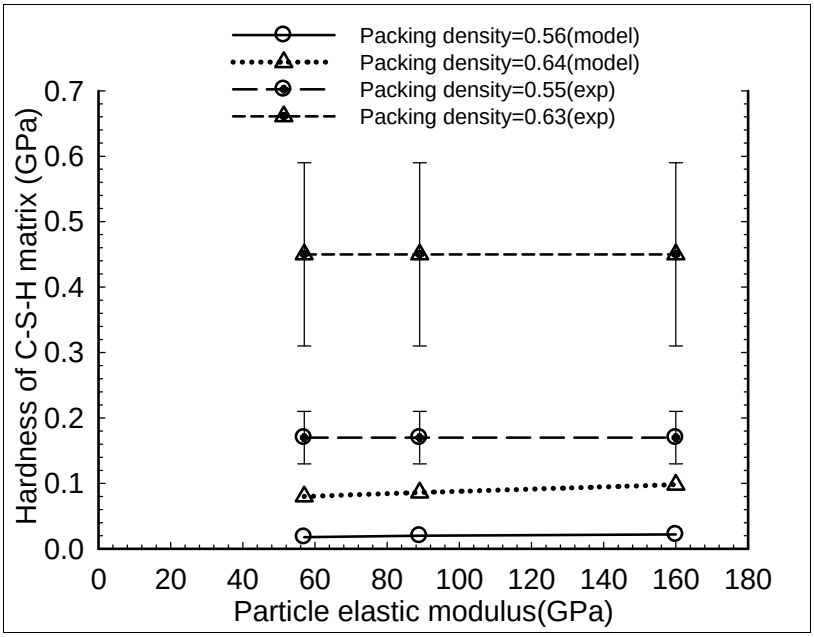

Figure 25. Hardness of C-S-H matrix is estimated from the data in Figure 23.

3.6 A summary of the effects of different parameters on C-S-H matrix properties

In the previous sections, the effects of rotational resistance, normal cohesive force, sliding friction coefficient, and particle elastic modulus on the elastic modulus and hardness of C-S-H matrix were discussed. To

develop a parameter space in which to improve the material properties of C-S-H matrix, the normalized increases in elastic modulus and hardness of C-S-H matrix were plotted with respect to the normalized increases in packing density, rotational stiffness, cohesive normal force, sliding friction coefficient, and particle elastic modulus in Figure 26. Figure 26 only includes the results for a packing density 0.64, which corresponds to the packing density of low-density C-S-H because the results for a packing density 0.74 show crack formation. The x and y coordinates in Figure 26 were estimated from those in Figures 15, 16, 18, 19, 21, 22, 24 and 25.

For the increase in packing density, the rotational stiffness was chosen to be 10 nN.nm/rad while other parameters in Table 1 remained unchanged except for packing density. A perusal of the Figure 25 indicates the following.

- Increasing packing density has the greatest effects on both elastic modulus and hardness of C-S-H matrix.
- Increasing particle elastic modulus has little effects on the hardness of C-S-H matrix but has moderate effects on the elastic modulus of C-S-H matrix.
- Increasing the rotational stiffness has the least effects on both elastic modulus and hardness of C-S-H matrix.
- Increasing cohesive normal force or sliding friction coefficient have moderate effects on the elastic modulus and hardness of C-S-H matrix.

The inordinate effect of packing density is likely the result of the increase in load-carrying inter-particle contacts that leads to a spreading of the load. Thus, making more efficient use of contact resistance by increasing the solid density appears to be more efficient than attempting to increase the contact strength or particle stiffness. The analysis does suggest that normal cohesive forces above those predicted from van der Waals and ionic correlation forces are probably present in C-S-H as suggested by Pellenq et al. (2008). Although some rolling resistance is necessary in the model to account for the likely non-spherical particle shapes, increasing rolling resistance by changing particle morphology is an inefficient approach to improving properties of C-S-H matrix. However, to the extent that changing morphology improves the inter-particle contacts or continuity, morphology can play a key role in improving C-S-H strength.

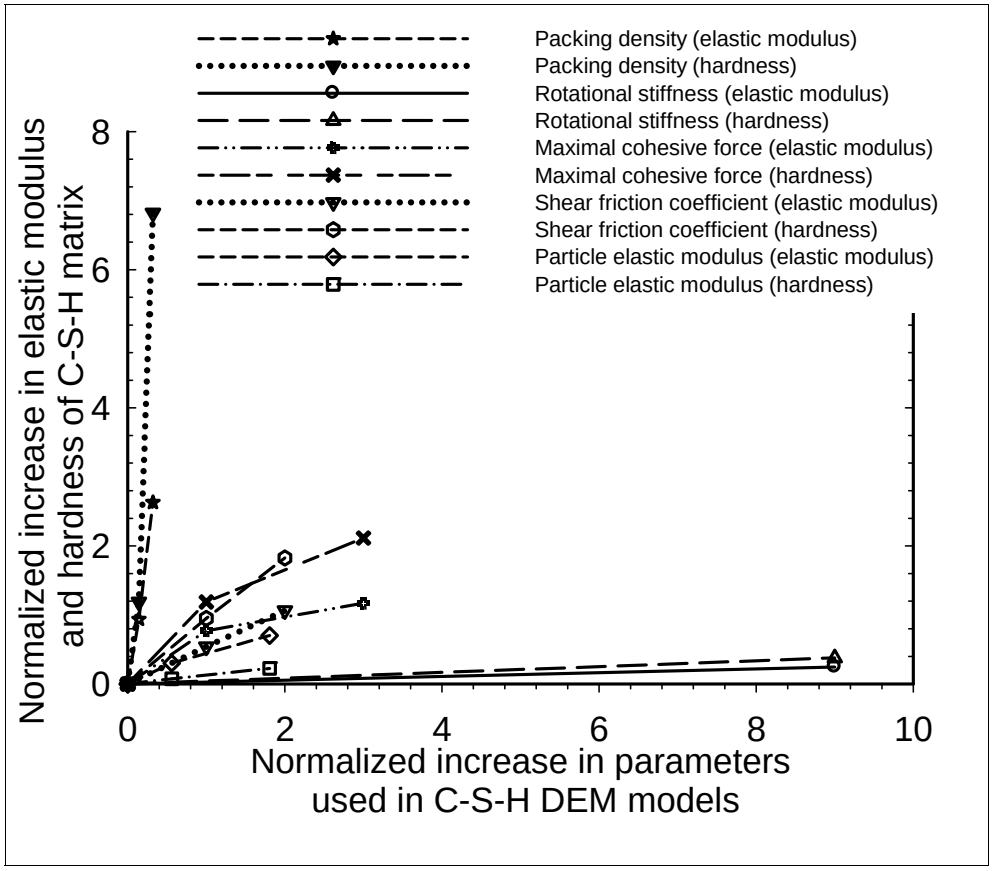

Figure 26. The normalized increase in elastic modulus and hardness versus the normalized increase in packing density, cohesive force, sliding friction coefficient, rotational stiffness and particle elastic modulus.

3.7 Conclusion

A parametric study was performed to study the effects of C-S-H nanoparticle morphology, interparticle forces, and particle properties on the elastic modulus and hardness of C-S-H matrix. The results show that increasing packing density is the most effective way to increase the stiffness and strength of C-S-H matrix. Ways to improve efficiency of load transfer through the nano-granular matrix through increased density of particle morphology appear to be more efficient than attempting to improve inter-particle resistance or particle stiffness.

4 Summary

Nanoindentation of C-S-H matrix material was modeled using the DEM method. Initial simulations based on the best estimate of material parameters showed good agreement with trends in the experimental data. However, the magnitudes of elastic modulus and hardness from the simulations were consistently lower for all packing densities considered. A parametric study was performed to determine which parameters could be varied to obtain reasonable agreement between simulation and experiment results. The rotational resistance between particles was found to be a key parameter because a relatively small additional rotational resistance brought the simulated curves more in line with experimental curves, yet the effect of rotational resistance quickly diminished for higher values. This finding was important because, unlike other parameters used in the model, rolling resistance cannot be measured by an independent experiment. In effect, the use of rolling resistance attempts to account for a geometric effect by endowing the material with a fictitious material attribute. It was anticipated that some rotational resistance was needed to make the ideal spheres used in the simulation behave more like the globular morphology posited for the actual material. Second, the insensitivity of results to large values of rotational resistance means that, while some rotation is both expected and effective in bringing the simulations in line with experiment results, having an accurate estimate of its value is not imperative. The effect of particle shape should be investigated in future studies.

Adding a cohesive normal force term to the interparticle resistance increased both the resistance and stiffness of the material. Similarly, increasing tangential resistance by an increased friction coefficient increased both strength and stiffness. Neither parameter had a large effect on elastic modulus and hardness. The particle elasticity had a limited effect on the simulation results.

The packing state had a greater effect on the nanoindentation behavior than all other parameters considered. This finding implies that increasing the packing state is more effective in increasing the engineering performance of C-S-H than attempting to alter composition of the particles.

References

Allen, A.J., J.J. Thomas, and H.M. Jennings. 2007. Composition and density of nanoscale calcium-silicate-hydrate in cement. Nature material(6):,311-315.

Allison, P. G., R.D. Moser, M.Q. Chandler, T.S. Rushing, B.A. Williams, and T.K. Cummins. 2011. Nanomechanical structure-property relations of dynamically loaded reactive powder concrete. Materials Characterization V: Computational Methods and Experiments (WIT Transactions on Engineering Sciences)(72): 287-298..

Anandarajah, A. 1994. Discrete Element Method for Simulating Behavior of Cohesive Soil. J. Geotech. Eng., 120(9): 1593-1613.

Cargile, James D. and L.E. Tidwell. 1993. Penetration of a Subscale Semi-Armor-Piercing Projectile into Conventional-Strength and High-Strength Concrete Targets. Technical Report SL-93-2, US Army Corps of Engineers, Waterways Experiment Station.

Constantinides, Georgios., F. –J. Ulm. 2007. The nanogranular nature of C-S-H. Journal of the mechanics and physics of solids (55): 64-90.

Constantinides, G., F.-J.Ulm, and K. Van Vliet. 2003. Materials and Structures/ Mat6riaux et Constructions(36): 191-196.

Cundall, P. A. 1971. A computer model for simulating progressive large scale movements in blocky rock systems. Proc. Symp. Int. Soc. Rock Mech.

Dejong, M.J. and F.J. Ulm. 2007. The nanogranular behavior of C-S-H at elevated temperatures (up to 700°C). Cement and Concrete Research 37(1): 1-12.

Davydov, D., M. Jirásek, L. Kopecký. 2011. Critical aspects of nano-indentation technique in application to hardened cement paste. Cement and Concrete Research(41): 20-29.

Ewald, P. 1921. Die Berechnung optischer und elektrostatischer Gitterpotentiale. Ann. Phys(369): 253–287.

Feiler, A., I. Larson, P. Jenkins, and P. Attard. 2000. A Quantitative Study of Interaction Forces and Friction in Aqueous Colloidal Systems. *Langmuir*(16): 10269-10277.

Gatty, L., S. Bonnamy, A. Feylessoufi, C. Clinard, P. Richard, and H. Van Damme. 2001. A transmission electron microscopy study of interfaces and matrix homogeneity in ultra-high-performance cement-based materials. Journal of materials science 36: 4013-4026.

Gauffinet, S., E. Finot., E. Lesniewska, and A. Nonat. 1998, Direct Observation of the Growth of Calcium Silicate Hydrate on Alite and Silica Surfaces by Atomic Force Microscopy. C. R. Acad. Sci. Paris, Earth and Planetary Science(327): 231-236.

Gmira, A., M. Zabat,, R. J. –M Pellenqand H. Van Damme,., 2004, Microscopic Physical Basis of the Poromechanical Behavior of Cement-based Materials, Mater. & Struct., Concr. Sci. Eng(37): 3-14.

Hamaker, H. C. 1937. The London-Van der Waals Attraction Between Spherical Particles. Physica IV(10): 1058-1072.

Horstemeyer, M. F., M.I. Baskes, S.J. Plimpton. 2001. Length scale and time scale effects on the plastic flow of FCC metals. Acta Materialia (49): 4363

Jennings, Hamlin M., 2000, A model for the Microstructure of Calcium Silicate Hydrate in Cement Paste, Cement and Concrete Research, (30): 101-116.

Jennings, Hamlin M., Jeffrey J.Thomas, Julia S. Gevreno , Georgios Constantinides, Franz-Josef Ulm. 2007. A multi-technique investigation of the nanoporosity of cement paste. Cement and Concrete Research (37): 329-336.

Jönsson, Bo, A. Nonat, C. Labbez, B. Cabane, and H. Wennerström. 2005. Controlling the Cohesion of Cement Paste. Langmuir (21): 9211-9221.

Manzano,H., J.S, Dolado, J, A. Ayuela, A 2009. Elastic properties of the main species present in Portland cement pastes. Acta Materialia 57: 1666-1674.

Mondal, Paramita, Shah, P. Surendar. 2006. Proceedings of ACI Session on Nanotechnology of Concrete: Recent Developments and Future Perspectives. Denver, USA.

Nonat, André 2004. The structure and stoichiometry of C-S-H, Cement and Concrete Research 34: 1521-1528.

Plassard, Cédric, Eric Lesniewska, Isabelle Pochard and André Nonat. 2005. Nanoscale Experimental Investigation of Particle Interactions at the Origin of the Cohesion of Cement. *Langmuir*(21): 7263-7270.

Pellenq, R.J.-M., N. Lequeux, and H. van Damme. 2008. Engineering the bonding scheme in C–S–H: The iono-covalent framework. Cement and Concrete Research (38): 159–174.

Pellenq, R.J. –M, Kushima, A., Shahsavari, R., Van liet, K.J.., Buehler, M.J., Yip, S., Ulm, F. J., 2009, A realistic molecular model of cement hydrates, Proceedings of the National Academy of Science 106(38): 16102-16107

Pellenq, R.J. –M and Van Damme, Henri., 2004, Why Does Concrete set?: The nature of Cohesion Forces in hardened Cement-Based Materials. MRS Bulletin: 319-323.ichardson, I. G., 2004, Tobermorite/jennite- and tobermorite/calcium hydroxide-based models for the structure of C-S-H: applicability to hardened pastes of tricalcium silicate, Portland cement, and blends of Portland cement with blast-furnace slag, metakaolin, or silica fume. Cement and Concrete Research 34(9):1733-1777.

Shan, Zhiwei, E.A. Stach, J.M.K. Wiezorek, J.A. Knapp, D.M. Follstatedt, and S.X. Mao. 2004. Grain Boundary-Mediated Plasticity in Nanocrystalline Nickel. Science(305): 654-656.

Sen, Dipanjan and Markus J.Buehler. 2009. Size and Geometry Effects on Flow Stress in Bioinspired De novo Metal-matrix Nanocomposites(11): 1-8.

Sorelli, Luca, Georgios Constantinides, Franz-Josef Ulm, François Toutlemonde. 2009. The nano-mechanical signature of Ultra High Performance Concrete by statistical nanoindentation techniques, 38(12): 1447-1456.

Ulm, Fran-Josef, Matthieu Vandamme, Chris Bobko, and Jose Alberto Ortega. 2007. Statistical Indentation Techniques for Hydrated Nanocomposites: Concrete, Bone, and Shale. J. Am. Ceram. Soc., 90(9): 2677-2692.

Wu, Jianzhong. and John M. Prausnitz. 2002. Generalizations for the Potential of Mean Force between Two Isolated Colloidal Particles from Monte Carlo Simulations. Journal of Colloid and Interface Science(252): 2326-2330.

Yao, M. and A. Anandarajah, 2003, Three-Dimensional Discrete Element Method of Analysis of Clays, Journal of Engineering Mechanics, ASCE: 585-596.

REPORT DOCUMENTATION PAGE

Form Approved
OMB No. 0704-0188

1. REPORT DATE *(DD-MM-YYYY)*	**2. REPORT TYPE**	**3. DATES COVERED** *(From - To)*
August 2012	Final Report	

4. TITLE AND SUBTITLE

Modeling Nanomechanical Behavior of Calcium-Silicate-Hydrate

5a. CONTRACT NUMBER

5b. GRANT NUMBER

5c. PROGRAM ELEMENT NUMBER

6. AUTHOR(S)

Mei Qiang Chandler, John F. Peters, and Daniele Pelessone

5d. PROJECT NUMBER
149289

5e. TASK NUMBER

5f. WORK UNIT NUMBER

7. PERFORMING ORGANIZATION NAME(S) AND ADDRESS(ES)

Geotechnical and Structures Laboratory
U.S. Army Engineer Research and Development Center
3909 Halls Ferry Road
Vicksburg, MS 39180

8. PERFORMING ORGANIZATION REPORT NUMBER

ERDC/GSL TR-12-30

9. SPONSORING / MONITORING AGENCY NAME(S) AND ADDRESS(ES)

10. SPONSOR/MONITOR'S ACRONYM(S)

11. SPONSOR/MONITOR'S REPORT NUMBER(S)

12. DISTRIBUTION / AVAILABILITY STATEMENT
Approved for public release; distribution is unlimited.

13. SUPPLEMENTARY NOTES

This study was conducted under the Military Engineering Basic Research Program, Project Number, 149289, "Multiscale Modeling of Structure of Materials," sponsored by Headquarters, U.S. Army Corps of Engineers.

14. ABSTRACT

The Discrete Element Method (DEM) was used to model the nanomechanical behavior of Calcium-Silicate-Hydrate (C-S-H). The inter-particle forces consist of the traditional friction and contact forces that operate in granular materials, with the addition of nanometer-scale forces between gels, including van der Waals and ionic correlation forces. The contact normal forces were based on the Hertz contact law. The van der Waals attractive forces were calculated based on Hamaker's equation. The ionic correlation forces, generated from the negative charges on the C-S-H gel surface and the ion species in the pore solution, were calculated using Monte Carlo (MC) simulations. The particles are spherical with diameters of approximately five nano-meters. Virtual nanoindentation was performed to evaluate the elastic modulus and hardness of C-S-H nanoparticle assemblies. Both elastic modulus and hardness, calculated from DEM, were much smaller than the results from nanoindentation experiments for corresponding C-S-H nanoparticle packing densities. By using a higher rotational stiffness, both bulk modulus and hardness increase and they match well with the experimental data, pointing to the possibility that the morphology of C-S-H is far from a perfect sphere and interlocking between particles provides significant strength to C-S-H. These studies show that the elastic modulus of a C-S-H matrix increases with increased packing ratio and rotational resistance, and its hardness increases with increased packing ratio, cohesion, rotational resistance and shear friction coefficient. The studies also show that the elastic properties of an individual C-S-H nanoparticle have little effect on the elastic modulus and hardness of the C-S-H matrix. The studies suggest that increasing packing density of the C-S-H nanostructure is a favorable way of making the C-S-H matrix stiffer. Increasing packing density, the cohesion and shear friction coefficient is effective in making the C-S-H matrix stronger. However, increasing packing density also makes the material response more brittle.

15. SUBJECT TERMS

Calcium-Silicate-Hydrate	Elastic modulus	Monte Carlo
Discrete Element Method	Hardness	Nanoparticle
	Interparticle forces	Packing density

16. SECURITY CLASSIFICATION OF:			**17. LIMITATION OF ABSTRACT**	**18. NUMBER OF PAGES**	**19a. NAME OF RESPONSIBLE PERSON: Mei Qiang Chandler**
a. REPORT	**b. ABSTRACT**	**c. THIS PAGE**			**19b. TELEPHONE NUMBER** *(include area code)*
Unclassified	Unclassified	Unclassified	Unclassified	50	(601) 634-4618